Check for updates

# Construction of magnetic MoS$_2$/NiFe$_2$O$_4$/MIL-101(Fe) hybrid nanostructures for separation of dyes and antibiotics from aqueous media†

Mehri Moradi-Bieranvand,[a] Saeed Farhadi, [ID] *[a] Abedin Zabardasti*[a] and Farzaneh Mahmoudi[b]

In this study, MoS$_2$/NiFe$_2$O$_4$/MIL-101(Fe) nanocomposite was synthesized by hydrothermal method and used as an adsorbent for the elimination of organic dyes and some antibiotic drugs in aqueous solutions. The synthesized nanocomposite underwent characterization through different techniques, including scanning electron microscopy (FE-SEM), energy-dispersive X-ray spectroscopy (EDX), Brunauer–Emmett–Teller (BET) surface area analysis, Fourier transform infrared (FT-IR) spectroscopy, X-ray diffraction (XRD), zeta potential analysis, vibrating sample magnetometry (VSM), and UV-vis diffuse reflectance spectroscopy (UV-vis DRS). These results demonstrated the successful insertion of MoS$_2$ within the cavities of MIL-101(Fe). The as-prepared magnetic nanocomposite was used as a new magnetic adsorbent for removing methylene blue (MB) and rhodamine B (RhB) organic dyes and tetracycline (TC) and ciprofloxacin (CIP) antibiotic drugs. For achieving the optimized conditions, the effects of initial pH, initial dye and drug concentration, temperature, and adsorbent dose on MB, TC, and CIP elimination were investigated. The results revealed that at a temperature of 25 °C, the highest adsorption capacities of MoS$_2$/NiFe$_2$O$_4$/MIL-101(Fe) for MB, TC, and CIP were determined to be 999.1, 2991.3, and 1994.2 mg g$^{-1}$, respectively. The pseudo-second-order model and Freundlich model are considered suitable for explaining the adsorption behavior of the MoS$_2$/NiFe$_2$O$_4$/MIL-101(Fe) nanocomposite. The magnetic nanocomposite was very stable and had good recycling capability without any change in its structure.

## 1. Introduction

The industrialization of the modern world and the increase in population have caused many environmental problems. Various inorganic and organic contaminants, including heavy metals, dyes, endocrine-disrupting compounds, pharmaceuticals, and personal care products, have often been detected in numerous drinking water sources and wastewaters worldwide.[1,2] Organic dyes are commonly utilized across multiple industries, including textiles, pharmaceuticals, cosmetics, medicine, paper, and leather.[3,4] Dye pollutants are highly toxic and do not break down easily. After these pollutants enter the water environment, they affect the lives of living organisms and cause diseases such as kidney and bladder cancer, as well as damage to nervous tissues.[5,6] Dye molecules have a very complex and stable structure and cause various diseases.[7,8] Another group of water pollutants are antibiotics.[9] Antibiotics, antihypertensive drugs, and pain-killers are excreted in the form of urine and faces, so a large amount of their residues can be seen in sewage effluents, soil, surfaces, and underground water.[10–13] Two types of well-known, available, and inexpensive antibiotics that are prescribed to fight infectious diseases, bacteria, fungi, and parasites in humans, livestock, and poultry are tetracycline and ciprofloxacin, which can be detected in aquatic environments.[14–17] The presence of these compounds, due to their metabolic properties, lack of decomposition, and accumulation in the environment, has caused serious problems in the lives of biological species. Therefore, it is very important to remove such compounds from water sources. In this regard, the design and synthesis of new and efficient adsorbents for efficient elimination of pollutants from wastewater is an attractive target.

There are various methods to remove organic dyes and antibiotic compounds, including photocatalysis,[18,19] Fenton reaction, surface adsorption,[20] advanced oxidation,[21] and biological treatment.[22] The method of surface adsorption is suitable as an effective process to remove these impurities from water. For the adsorption process, clay, graphene oxide, carbon nanotubes, and biochar have been used as adsorbents.[23–25] Other compounds, such as TiO$_2$, ZnO, and molybdenum disulfide (MoS$_2$), can also be

[a] Department of Inorganic Chemistry, Faculty of Chemistry, Lorestan University, Khorramabad, 68151-44316, Iran. E-mail: farhadi.s@lu.ac.ir; sfarhadi1348@yahoo.com; zabardasti.a@lu.ac.ir

[b] Department of Chemistry, University of Miami, Coral Gables, Florida 33146, USA
† Electronic supplementary information (ESI) available. See DOI: https://doi.org/10.1039/d4ra00505h

used as adsorbents to remove aqueous pollutants. Among the reported adsorbents, the two-dimensional 2D $MoS_2$ material can be very promising due to its high oxidation ability, chemical stability, and adjustable distance between layers.[26–29] These characteristics have made this compound suitable for use in the manufacture of lubricants, the manufacture of lithium and sodium batteries, and in nana devices.[30,31] The main problem of with composition is the limited number of active sites attributed to the van der Waals interactions in the layered crystals, which facilitate the aggregation of $MoS_2$ nanosheets. In order to overcome these constraints, researchers have employed metal–organic frameworks (MOFs) to augment the characteristics of $MoS_2$. MOFs have garnered significant interest in adsorption and separation applications owing to their extensive pore structures.[32–35] MOFs are porous and crystalline materials that consist of a metal component and an organic ligand and have a large emission area and very high porosity. MOFs have gained significant recognition as an excellent adsorbent for efficiently eliminating pollutants. These MOFs possess remarkable environmental compatibility and exhibit minimal toxicity, making them highly suitable for pollution removal purposes. Coupling $MoS_2$ with MOF porous structure significantly increases the ability to remove pollutants from aqueous environments.[36–39] However, these MOF-based composites are not easily recyclable in aqueous environments. For convenient separation of these compounds, they can be combined with magnetic nanoparticles such as nickel ferrite. Utilizing an external magnet, magnetic separation presents a direct approach to improve the recyclability of samples.

In this research, $MoS_2$ nanosheets with a flower-like morphology were integrated into the MIL-101(Fe) metal organic framework along with $NiFe_2O_4$ magnetic nanoparticles to create a novel magnetically recoverable $MoS_2/NiFe_2O_4/MIL$-101(Fe) ternary nanocomposite. The structure and morphological features of the nanocomposite were thoroughly investigated using various techniques. The $MoS_2/NiFe_2O_4/MIL$-101(Fe) nanocomposite exhibited remarkable effectiveness in adsorbing a wide range of environmental contaminants like methylene blue (MB), methyl orange (MO), and rhodamine B (RhB), as well as pharmaceutical compounds like tetracycline (TC) and ciprofloxacin (CIP) from water solutions. Moreover, the nanocomposite can be effortlessly extracted from the reaction setup using an external magnet. These findings highlight the potential of the synthesized nanocomposite in the treatment of wastewater contaminated with organic pollutants.

## 2. Experimental

### 2.1. Materials

Terephthalic acid ($H_2BDC$, 98%), iron(III) chloride hexahydrate ($FeCl_3 \cdot 6H_2O$, 99%), $N,N$-dimethylformamide (DMF, 99%), sodium hydroxide (NaOH, 98%), nickel(II) nitrate hexahydrate ($Ni(NO_3)_3 \cdot 6H_2O$, 98%), iron(III) nitrate nonahydrate ($Fe(NO_3)_3 \cdot 9H_2O$, 98%), thiourea ($CH_4N_2S$, 98%) (99%), sodium molybdate ($Na_2MoO_4 \cdot 2H_2O$, 98%), oxalic acid ($C_2H_2O_4 \cdot 2H_2O$, 98%), methylene blue (MB, $C_{16}H_{18}ClN_3S$, 99%), methyl orange (MO, $C_{14}H_{14}N_3NaO_3S$, 99%), rhodamine B (RhB, $C_{28}H_{31}ClN_2O_3$, 99%) were provided from Merck Chemical Co. and tetracycline (TC,

99.5%), ciprofloxacin (CIP, 95.5%) drugs were obtained from Exir pharmaceutics Co. (Boroujerd, Iran).

### 2.2. Synthesis of flower-like $MoS_2$ nanosheets

The $MoS_2$ sample was prepared using the hydrothermal method. 4 mmol of sodium molybdate ($Na_2MoO_4 \cdot 2H_2O$) was dissolved with 15 mmol of thiourea ($CH_4N_2S$) and 3 mmol of oxalic acid in ($C_2H_2O_4 \cdot 2H_2O$) 40 mL of deionized water and stirred for 3 hours. Then the clear solution was transferred into a Teflon-lined autoclave and placed in an oven at 200 °C for 24 hours. The autoclave was cooled to room temperature, and then the precipitate was dried in an oven at 80 °C for 4 hours.

### 2.3. Synthesis of magnetic $NiFe_2O_4$ nanoparticles

By employing the hydrothermal method, nickel-ferrite ($NiFe_2O_4$) nanoparticles were successfully synthesized. Fe ($NO_3)_3 \cdot 9H_2O$ (1.62 g) and Ni ($NO_3)_2 \cdot 6H_2O$ (0.705 g) were combined with 25 mL of distilled water and stirred for 30 min, then 10 mL of a 6 M NaOH solution was added. The suspension was stirred for 1 hour. Then, it was transferred to an autoclave lined with Teflon and subjected to a temperature of 200 °C for 24 hours. The autoclave was cooled to room temperature. The sediment obtained was washed several times with water and ethanol to remove impurities. Then, it was placed in an oven at a temperature of 60 °C for 12 hours to dry.

### 2.4. Fabrication of magnetic $MoS_2/NiFe_2O_4/MIL$-101(Fe) nanocomposite

For the fabrication of $MoS_2/NiFe_2O_4/MIL$-101(Fe) magnetic adsorbent, $FeCl_3 \cdot 6H_2O$ (1.35 g), $H_2BDC$ (0.415 g), $MoS_2$ (0.6 g), and $NiFe_2O_4$ (0.25) g were mixed with 30 mL of DMF, and it was stirred for 30 minutes. Then the resulting suspension was transferred to a Teflon-lined autoclave and placed at a temperature of 120 °C for 20 hours. The autoclave was cooled to room temperature. After washing several times with DMF, the resulting precipitate was dried in an oven at a temperature of 60 °C (Fig. 1).

### 2.5. Characterization

FT-IR spectra were recorded using a Shimadzu-8400S spectrometer (Japan) in the wavenumber range of 400–4000 $cm^{-1}$. The structure and level of crystallinity of samples were determined by using a Philips 8440 X-Pert X-ray diffractometer (Netherland), operating at 40 mA and 40 kV with copper radiation ($k = 0.1542$ nm). UV-vis spectra were recorded on a Carry 100 Varian spectrophotometer (USA). $N_2$ adsorption–desorption isotherms and BJH pore-size distribution plots of samples were determined by using a Micro metrics PHS-1020 instrument (Japan) at 77 K. The degassing process of samples was performed at 150 °C. The magnetic properties of samples at 27 °C within the range of ±15 000 Oe was carried out using a vibrating magnetometer (Iran). The surface charge of the materials was investigated by zeta potential measurements on a HORIBA Scientific Zetasizer (Japan). A MIRA3 TESCAN scanning electron microscope (Czech) was employed to examine the morphology
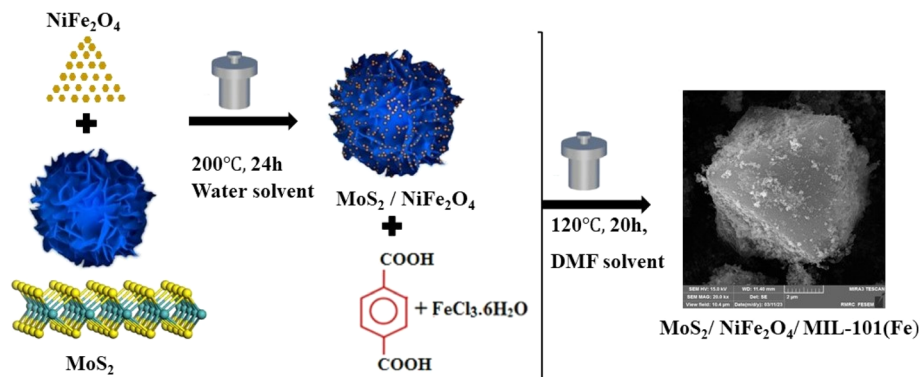
**Paper**

**RSC Advances**

**Fig. 1** The preparation process of MoS$_2$/NiFe$_2$O$_4$/MIL-101(Fe) nanocomposite.

of the prepared materials, while X-ray energy analysis (EDX) was utilized for elemental analysis of the samples.

## 2.6. Dye absorption tests

In this investigation, the solutions of organic dyes (MB, RhB, and MO) were separately prepared in deionized water. The stock aqueous solutions had a concentration of 200 ppm. Subsequently, dilution was performed using these solutions. The absorbance spectra of MB, MO, and RhB dyes were monitored measured by a UV-vis spectrophotometer at wavelengths of 664, 463, and 554 nm, respectively. Various parameters including different dye concentrations, pH effects, temperature effects, and absorbent dosage were investigated. In order to assess the influence of the initial concentration, 25 mg of magnetic nanocomposite was poured into dye solutions of RhB, MB, and MO. The dye solutions had concentrations varying from 25 to 150 ppm, and a volume of 30 mL was used. To examine the impact of pH on the adsorption process, the initial pH of the MB solutions was adjusted by adding HCl (0.1 mol L$^{-1}$) for acidic conditions and NaOH (0.1 mol L$^{-1}$) for alkaline conditions in the range of 2–10. Furthermore, we investigated the effect of temperature on the adsorption process by conducting experiments at temperatures ranging from 25 to 65 °C.

To assess the composite's effectiveness, the solutions containing the magnetic adsorbent were collected using a magnet after each use. Afterwards, they were subjected to repeated washing with ethanol and DMF. After that, the adsorbent underwent a 24 hours drying process at 60 °C in an oven and was subsequently utilized for further testing. The equilibrium capacity of adsorption ($q_e$ in mg g$^{-1}$) and the percentage of removal ($R$ (%)) were obtained through the use of the following equations (eqn (1) and (2)):

$$q_e = (C_0 - C_e) \times V/m \tag{1}$$

$$R\ (\%) = (C_0 - C_e) \times 100/C_0 \tag{2}$$

Here, $C_0$ and $C_e$ (mg L$^{-1}$, ppm) symbolize the initial and ultimate concentrations of the pollutant, whereas $V$ (L) and $m$ (g) indicate the volume of the pollutant solution and the mass of the absorbent substance, respectively.

## 2.7. Drug adsorption tests

The magnetic MoS$_2$/NiFe$_2$O$_4$/MIL-101(Fe) nanocomposite was utilized to facilitate the adsorption process of TC and CIP drugs. In this study, various factors were investigated, including pH, temperature, adsorbent dose, and initial drug concentration. The temperature levels considered were 25, 35, 45, 55, and 65 °C. The acidic conditions studied included pH 2 and 4, while the neutral conditions were around pH 7, and the alkaline conditions were pH 8 and 10. The initial drug concentrations were categorized as low drug concentrations (25 mg L$^{-1}$), medium drug concentrations (50, 75, and 100 mg L$^{-1}$), and high drug concentrations (125 mg L$^{-1}$). The adsorbent doses were selected as 15, 25, 35 and 45 mg.

To examine the adsorption process, medicinal solutions of TC and CIP with a concentration of 200 mg L$^{-1}$ were prepared separately and subsequently diluted. Then, specific amounts of magnetic adsorbent were added to a 50 mL aqueous drug solution and stirred. Afterward, the medicinal solution was separated from the magnetic adsorbent. The concentrations of TC and CIP drugs were determined using UV-vis spectrophotometry at wavelengths of 373 and 337 nm, respectively. The pH of the solutions was adjusted by using HCl (0.1 mol L$^{-1}$) and NaOH (0.1 mol L$^{-1}$) aqueous solutions.

To investigate the impact of temperature on adsorption, a series of experiments were conducted at different temperatures, namely 25, 35, 45, 55, and 65 °C, in order to evaluate their respective effects. For every given temperature, 25 mg of magnetic adsorbent was used in a 50 mL drug solution. After each test, the magnetic adsorbent was separated from the drug solution using a magnet. It was then washed multiple times with DMF and ethanol before undergoing a 24 hours drying process in an oven set to 60 °C. To compute the adsorption capacities ($q_e$) of the two antibiotics, the above equations (eqn (1) and (2)) were employed.

## 3. Results and discussion

### 3.1. Characterization of the as-prepared samples

**3.1.1 FT-IR analysis.** FT-IR spectroscopy is a useful method for analyzing functional groups in organic and inorganic materials. Fig. 2 exhibits the IR spectra of NiFe$_2$O$_4$, MIL-
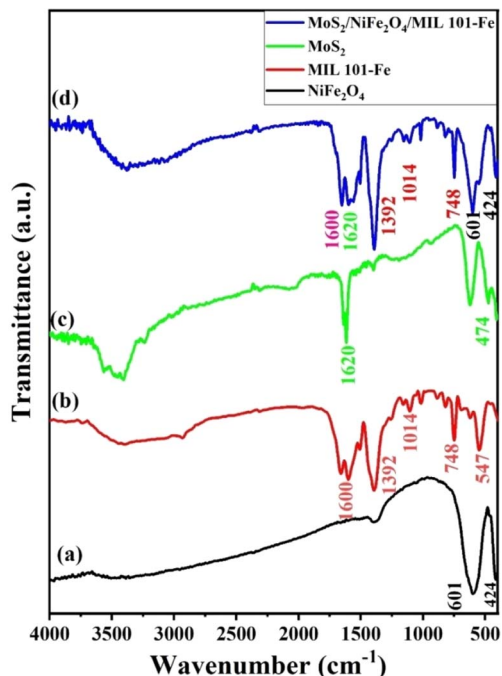
**Fig. 2** FT-IR spectra of (a) $NiFe_2O_4$, (b) MIL-101(Fe), (c) $MoS_2$, and (d) $MoS_2/NiFe_2O_4/MIL$-101(Fe).

101(Fe), $MoS_2$, and the $MoS_2/NiFe_2O_4/MIL$-101(Fe) composite samples over the range of 400–4000 $cm^{-1}$. The FT-IR spectrum of $NiFe_2O_4$ in Fig. 2(a) shows two bands at 601 and 424 $cm^{-1}$, which are attributed to the stretching vibrations of the metal–oxygen bond at the tetrahedral and octahedral sites in spinel structures, respectively.[40] The presence of characteristic peaks at 547, 748, 1014, 1392, and 1600 $cm^{-1}$ in Fig. 2(b) provides evidence for the successful synthesis of MIL-101(Fe).[41] The 1014 $cm^{-1}$ band was assigned to the C–O–C bending vibrations, whereas the 748 $cm^{-1}$ band was indicative of the C–H bending vibrations. Furthermore, the confirmation of the O–C=O asymmetric and symmetric vibrations at 1600 and 1392 $cm^{-1}$ reinforces the conclusions drawn in prior research.[42] Fig. 2(c) illustrates the FT-IR spectrum of $MoS_2$, where the presence of a peak at 474 $cm^{-1}$ indicates the characteristic S–S bond of $MoS_2$. Additionally, the spectrum exhibits prominent and distinct peaks at 3435 $cm^{-1}$ and 1620 $cm^{-1}$, corresponding to the stretching vibration of –OH groups and the existence of adsorbed water. These spectral characteristics provide valuable information regarding the molecular properties and environmental interactions of $MoS_2$.[43] In Fig. 2(d), the nanocomposite exhibits the existence of magnetic $NiFe_2O_4$ through distinctive bands in the range of 400–600 $cm^{-1}$.[44] Moreover, the emergence of bands around 1600 and 1392 $cm^{-1}$ can be attributed to the existence of carboxylate groups within the MIL-101(Fe) constituent. The intensity of the weak band at 474 $cm^{-1}$, which is attributed to the S–S bond of $MoS_2$, exhibits a decline after exposure to the composite. The observed attenuation of the S–S bond confirms the structural modifications occurring within the composite and validates the synthesis process.

**3.1.2 Powder X-ray diffraction (XRD).** The XRD analysis was used to analyze the crystallographic information of the materials synthesized. In Fig. 3, the XRD diffraction patterns of $NiFe_2O_4$, $MoS_2$, MIL-101(Fe), and the $MoS_2/NiFe_2O_4/MIL$-101(Fe) composite are displayed. Fig. 3(a) shows the XRD peaks of the synthesized $NiFe_2O_4$ nanoparticles. The structure of $NiFe_2O_4$ was cubic spinel. Sharp peaks appeared at $2\theta = 35.88°$ (311), whereas other peaks appeared at $2\theta = 30.47°$ (220), 38.06° (222), 43.44° (400), 53.75° (422), 57.31° (511), and 62.93° (440).[40] The XRD pattern of MIL-101(Fe) is depicted in Fig. 3(b), showing distinct diffractions at $2\theta$ values of 9.36°, 18.98°, and 23.70°, corresponding to the crystal planes (311), (511), and (852) of the MIL-101(Fe) phase.[42] Fig. 3(c) shows the XRD pattern of $MoS_2$ with peaks located at 13.64°, 32.36°, 35.57°, 43.46°, and 57.54°, corresponding to (002), (100), (102), (104), and (110) hexagonal crystallographic planes of $MoS_2$.[43] The XRD analysis of the $MoS_2/NiFe_2O_4/MIL$-101(Fe) composite in Fig. 3(d) demonstrates the existence of distinct peaks corresponding to $MoS_2$, $NiFe_2O_4$, and MIL-101(Fe). However, the characteristic peak intensity was obviously decreased, indicating the good dispersion of $MoS_2$ and $NiFe_2O_4$ in the MIL-101(Fe) MOF after the synthesis of the $MoS_2/NiFe_2O_4/MIL$-101(Fe) composite.

**3.1.3 Structural morphology.** The structural morphology and shape of the crystals were analyzed using field emission scanning electron microscopy (FESEM), and the corresponding images are shown in Fig. 4. For the case of $MoS_2$, as shown in Fig. 4(a) and (b), the nanosheets were agglomerated, forming hierarchical microspheres, with the $MoS_2$ nanosheets
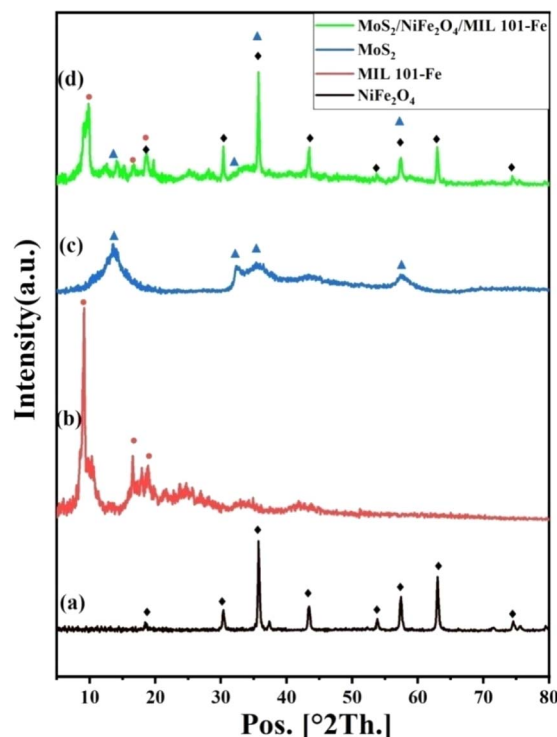


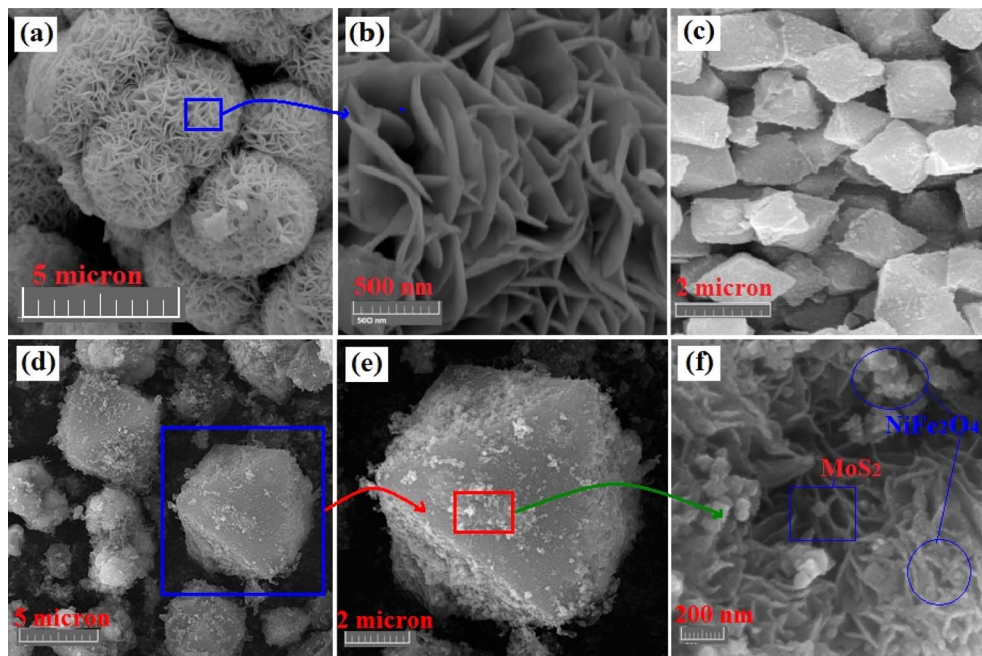**Fig. 3** XRD patterns of (a) $NiFe_2O_4$, (b) MIL-101(Fe), (c) $MoS_2$, and (d) $MoS_2/NiFe_2O_4/MIL$-101(Fe).

**Fig. 4** FESEM images of (a and b) $MoS_2$, (c) nascent MIL-101(Fe) MOF crystals, (d and e) $MoS_2/NiFe_2O_4$/MIL-101(Fe) ternary nanocomposite and (f) high-resolution image of $MoS_2$ patches on MIL-101(Fe) crystals.

(thickness: 5–10 nm) stacked in layers. As shown in Fig. 4(c), the nascent MIL-101(Fe) crystals have well-defined octahedral shapes with a diameter of 1–2 μm. This indicates uniform growth of the MOF crystals during hydrothermal synthesis, imparting regular crystallinity. Furthermore, for the nanocomposite in Fig. 4(d), the similar octahedral crystal structure was decorated with $MoS_2$ patches on the outer surface of the MOF crystals, with no alteration of the overall crystal shape or morphology. Indeed, the introduction of $MoS_2$ changed the sizes of the octahedrons from 1–2 μm to 5–10 μm with a rough surface. As can be seen in Fig. 4(e), the $MoS_2$ nanosheets were uniformly distributed and anchored on the surfaces of the MIL-101(Fe) crystals. From the high-resolution image of the $MoS_2$ patches on the outer surface of the composite in Fig. 4(f), it can be observed that the $NiFe_2O_4$ nanoparticles are well dispersed densely on the surface of sheet-like $MoS_2$ patches. The agglomerated patch-like growth of $MoS_2$ nanosheets imparts surface heterogeneity and defects, and this kind of structure is highly efficient for the introduction of a large number of active sites and boosting the adsorption process.

**3.1.4 EDX analysis.** Energy dispersive X-ray spectroscopy (EDX) is a powerful tools used to study the chemical composition of materials at the nanoscale. Analysis of the X-ray spectrum emitted from a sample can determine the elemental composition of the sample with high precision and accuracy. The EDX spectrum confirms the presence of various elements in the composite. The results of EDX mapping confirm the distribution of elements and the homogeneity of the samples. Fig. 5(a) confirmed the presence of multiple elements, including C, O, S, Fe, Ni and Mo elements within the composite. The table in the inset of Fig. 5(a) shows the quantitative

elemental analysis results of the $MoS_2/NiFe_2O_4$/MIL-101(Fe) nanocomposite. In addition, EDX elemental mappings of an octahedral crystal structure of the MIL-101(Fe) MOF decorated with $MoS_2$ and $NiFe_2O_4$ in Fig. 5(b) show that elements were uniformly distributed over the $MoS_2/NiFe_2O_4$/MIL-101(Fe) composite.

**3.1.5 Magnetic properties.** The magnetic parameters of $NiFe_2O_4$ nanoparticles and $MoS_2/NiFe_2O_4$/MIL-101(Fe) nanocomposite samples, including magnetic saturation ($M_S$), coercivity ($H_C$), and magnetic retardation ($M_r$), were obtained from their hysteresis curves. The hysteresis curves in Fig. 6 exhibit superparamagnetic behavior at room temperature, revealing the presence of small magnetic nanoparticles. The saturation magnetization ($M_S$) value for $MoS_2/NiFe_2O_4$/MIL-101(Fe) nanocomposite is about 11.52 emu $g^{-1}$, which is lower than that of pure $NiFe_2O_4$ nanoparticles (53.92 emu $g^{-1}$). The primary cause of this decrease can be attributed to the presence of nonmagnetic $MoS_2$/MIL-101(Fe) particles in the nanocomposite. As shown in the inset of Fig. 6, the synthesized nanocomposite still possesses a sufficient magnetization for easy and fast separation from the contaminated water using a magnet. Then, the magnetic property of the nanocomposite helps us to separate the particles easily after its use in the adsorption process.

**3.1.6 BET analysis.** By using the data related to $N_2$ adsorption–desorption on the $MoS_2/NiFe_2O_4$/MIL-101(Fe) nanocomposite at different relative pressures, useful information such as the volume, size, and size distribution of the pores was obtained, which is shown in Fig. 7 and Table 1. According to the classification of absorption isotherms based on IUPAC, in this study, type I and IV isotherms were seen, which are related to mesoporous materials. The BET surface areas calculated
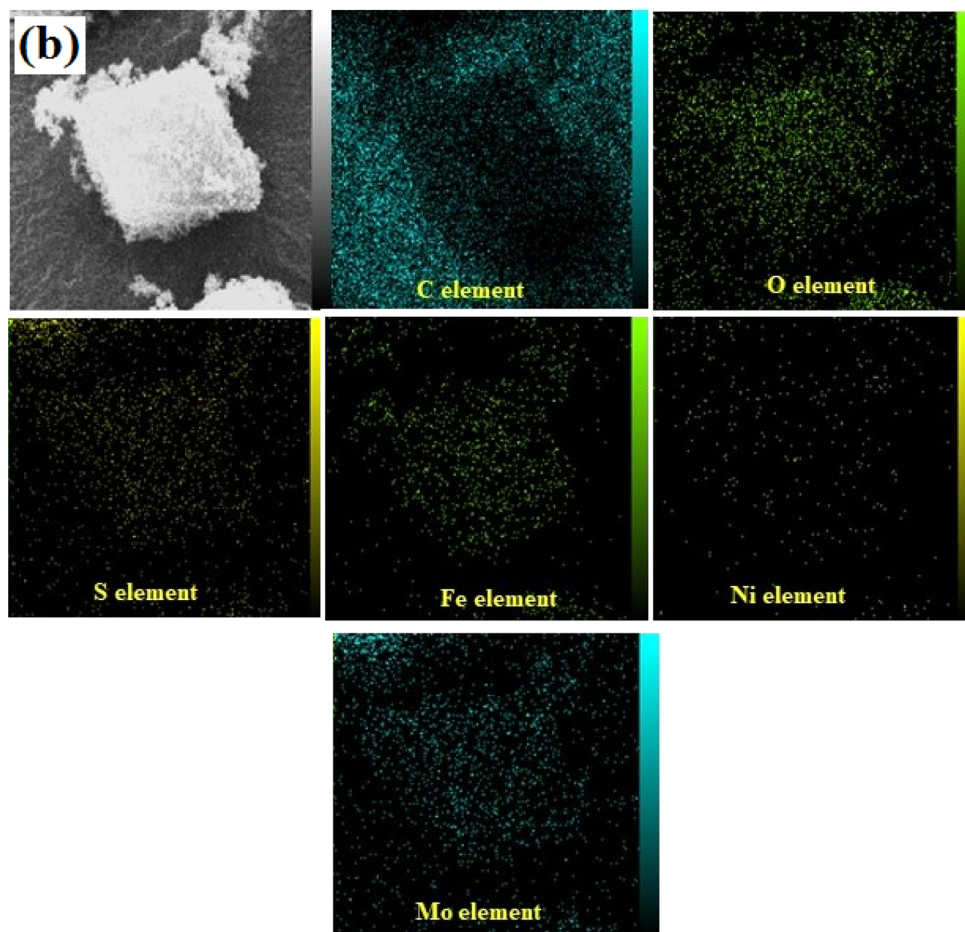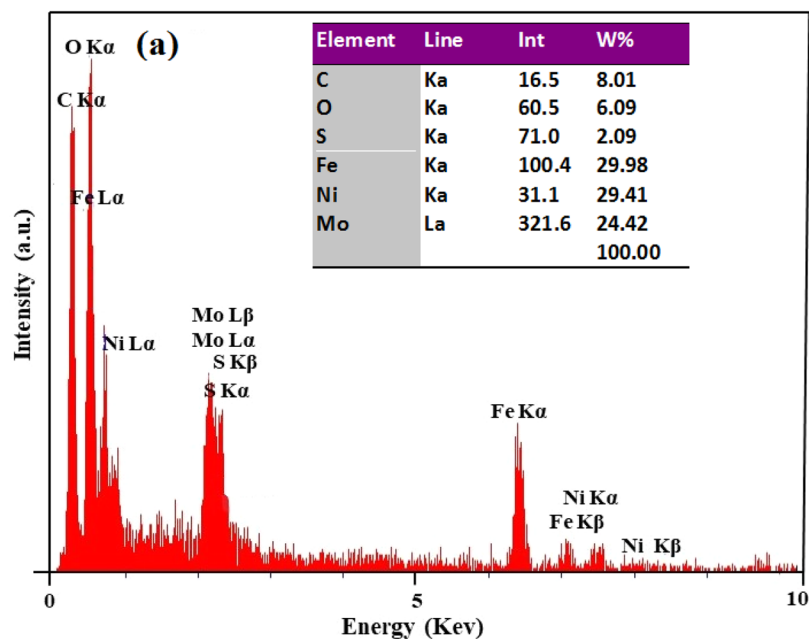
| Element | Line | Int | W% |
|---------|------|------|-------|
| C | Ka | 16.5 | 8.01 |
| O | Ka | 60.5 | 6.09 |
| S | Ka | 71.0 | 2.09 |
| Fe | Ka | 100.4 | 29.98 |
| Ni | Ka | 31.1 | 29.41 |
| Mo | La | 321.6 | 24.42 |
| | | | 100.00 |

**Fig. 5** (a) EDX spectrum and (b) an indicative SEM image of the $MoS_2/NiFe_2O_4/MIL-101(Fe)$ with corresponding elemental mappings.

from the isotherms are as follows: pure $MoS_2$ (3.5 m² g⁻¹), MIL-101(Fe) (167.0 m² g⁻¹), and $MoS_2/NiFe_2O_4/MIL-101(Fe)$ (29.2 m² g⁻¹). The Barrett–Joyner–Halenda (BJH) model provided information on the pore size distribution using the adsorption branch of the isotherm. The $MoS_2/NiFe_2O_4/MIL-101(Fe)$ composite exhibits a reduced surface area and pore volume

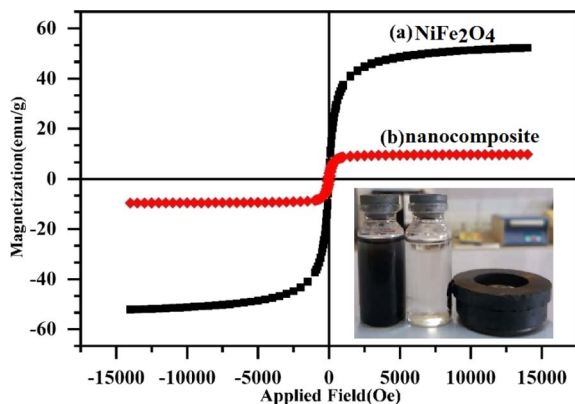**Fig. 6** Magnetization curves of (a) $NiFe_2O_4$ and (b) $MoS_2/NiFe_2O_4/$ MIL-101(Fe) samples.

compared to pure MIL-101(Fe). These decreases may be attributed to the incorporation of $MoS_2$, which has relatively lower BET surface area and pore volumes.

**3.1.7 Zeta potential measurements.** To analyse the surface potential properties of the acquired samples, the zeta potential was measured for each sample. The results can be seen in Fig. 8. The zeta potential values were measured as $-47.0$ mV for $MoS_2$ and $+32.4$ mV for MIL-101(Fe). In contrast, the charge distribution on the surface of the $MoS_2/NiFe_2O_4/MIL-101(Fe)$ composite was measured to be $-19.8$ mV. The notable shift of zeta potential for MIL-101(Fe) from $+32.4$ to $-19.8$ mV is primarily caused by the introduction of the highly negatively charged $MoS_2$ component into the framework of MIL-101(Fe). The increased negative charge of nanocomposite is related to the presence of $MoS_2$ component inside the porous framework of MIL-101(Fe), making it more suitable for the selective adsorption of cationic species *via* electrostatic interaction in water at natural pH.

## 3.2. Dye adsorption investigations

In an experimental study, we employed a novel method to assess the effectiveness of the $MoS_2/NiFe_2O_4/MIL-101(Fe)$ nanocomposite. Our focus was on testing this composite
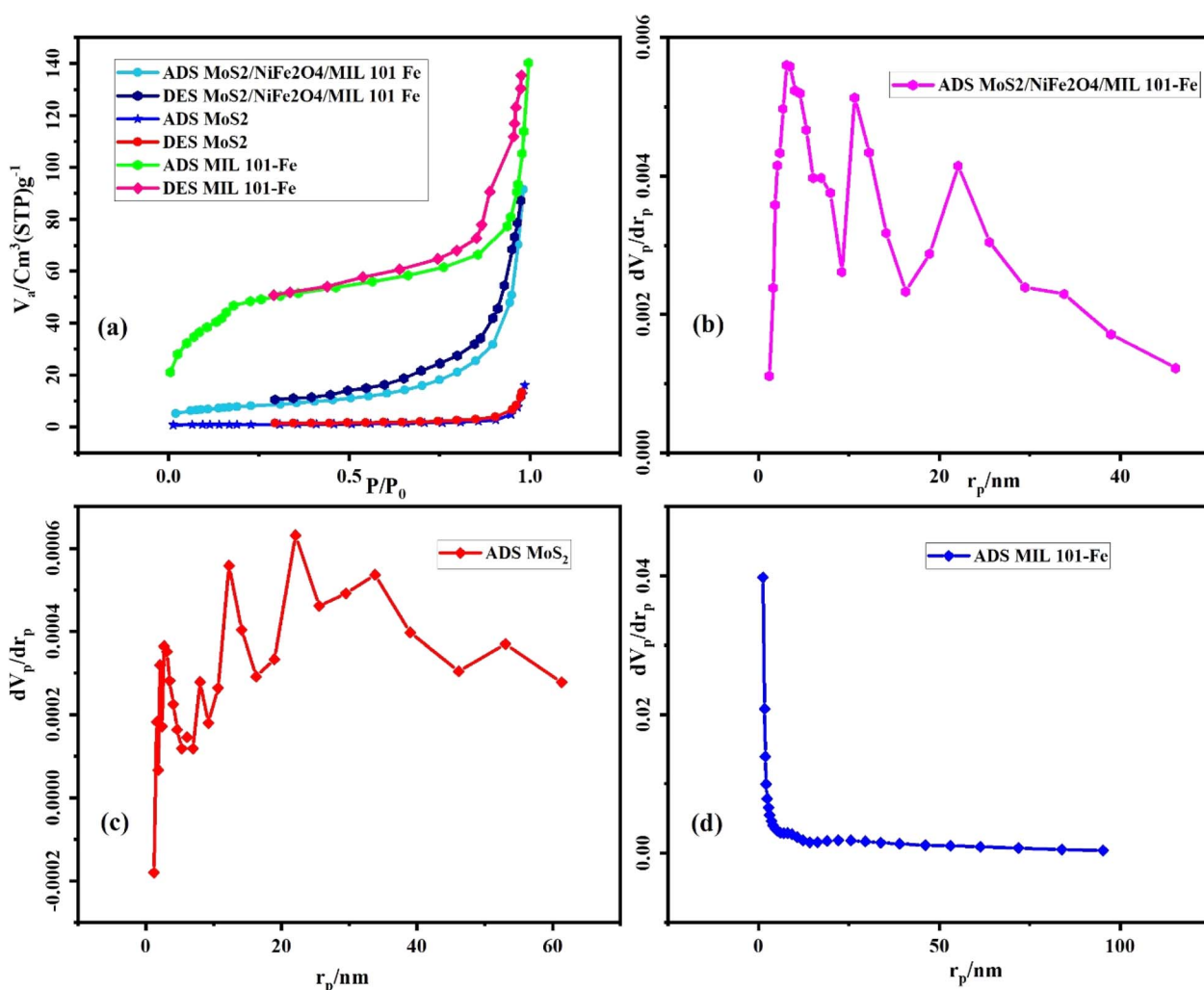


**Fig. 7** (a) $N_2$ adsorption–desorption isotherms and (b–d) BJH pore-size distribution plots for the $MoS_2/NiFe_2O_4/MIL-101(Fe)$, $MoS_2$ and MIL-101(Fe) samples.

**Table 1** The textural properties of as-prepared samples

| Sample | BET surface area ($S_{\text{BET}}$, m$^2$ g$^{-1}$) | Total pore volume ($V_{\text{p}}$, cm$^3$ g$^{-1}$) | Average pore diameter ($r_{\text{p}}$, nm) |
|---|---|---|---|
| MoS$_2$ | 3.5 | 0.024 | 28.40 |
| MIL-101(Fe) | 167.0 | 0.198 | 4.75 |
| MoS$_2$/NiFe$_2$O$_4$/MIL101(Fe) | 29.2 | 0.141 | 19.38 |

material's ability to remove various contaminants from water, specifically targeting compounds such as methylene blue (MB), rhodamine B (RhB), and methyl orange (MO). These compounds were chosen due to their diverse sizes and charges, providing a comprehensive evaluation of the nanocomposite's performance. UV-vis absorption spectra of MB, RhB, and MO dyes were recorded at $\lambda_{\text{max}}$ of 664, 553, and 463 nm, respectively. Fig. 9 depicts a gradual reduction in the intensity of these absorption bands, indicating a decrease in the concentration of dyes in the solution over time. The nanocomposite exhibited

a high adsorption efficiency of 98% for MB within 24 minutes (Fig. 9(a)), while the removal efficiency for RhB was approximately 36% within the same timeframe (Fig. 9(b)). However, the adsorption of MO was almost negligible (Fig. 9(c)). These results suggest that the MoS$_2$/NiFe$_2$O$_4$/MIL-101(Fe) magnetic nanocomposite possesses varying adsorption capacities for different organic dyes. Different dye molecules exhibit adsorption behavior that correlates with the negative charge found on the surface of the MoS$_2$/NiFe$_2$O$_4$/MIL-101(Fe) magnetic adsorbent. Consequently, the magnetic nanocomposite demonstrates favorable adsorption capabilities towards cationic dyes like MB and RhB. However, the removal percentage of RhB dye is lower than that of MB, probably due to the large volume of RhB molecules causing steric hindrance with adsorption sites on the composite surface and weaker $\pi$–$\pi$ interaction with MoS$_2$/NiFe$_2$O$_4$/MIL-101(Fe) nanocomposite. The results show that the nanocomposite is a poor adsorbent for the removal of MO anionic dye from aqueous solutions. It can be attributed to the negative charge of this dye molecule, which repels each other between MO and the MoS$_2$ caged in MIL-101. The slightly
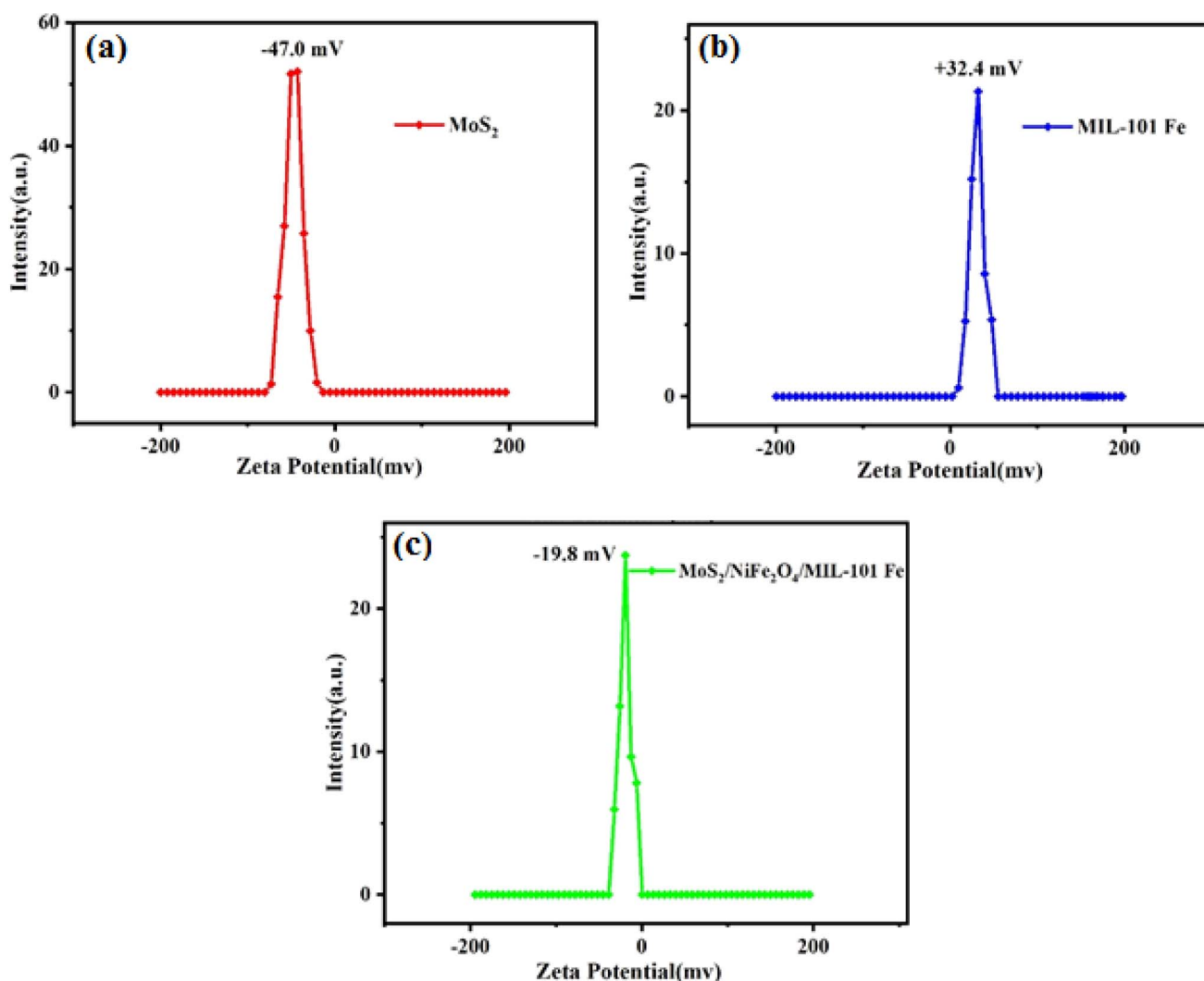


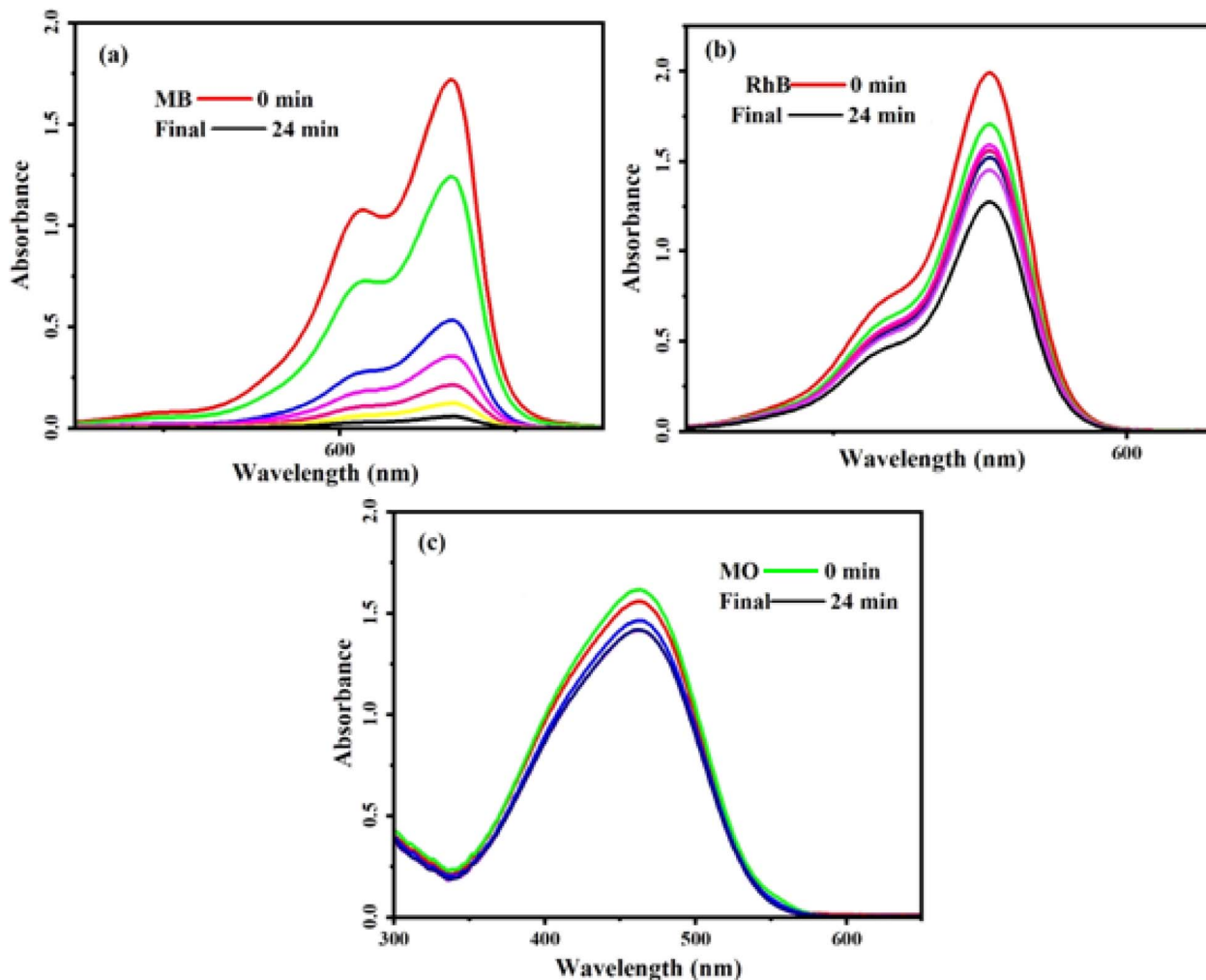**Fig. 8** Zeta potential curves of (a) MoS$_2$, (b) MIL-101(Fe) and (c) MoS$_2$/NiFe$_2$O$_4$/MIL-101(Fe).

**Fig. 9** The UV-vis spectra during adsorption of dyes over $MoS_2/NiFe_2O_4/MIL-101(Fe)$: (a) MB, (b) MO and (c) RhB. $C_0$ (dye) = 25 mg L$^{-1}$, $V$ (dye) = 30 mL, adsorbent dosage = 25 mg and temp. = 25 °C.

decreasing absorbance of MO is more likely to be adsorbed on the surface of adsorbents. The results further confirm that the electrostatic attraction is the key factor for the occurrence of adsorption.

**3.2.1 Effect of adsorbent dose on the dye adsorption.** The amount of adsorbent used plays a crucial role in determining both the level of dye adsorption and the effectiveness of dye elimination. In Fig. 10(a), the impact of different doses of $MoS_2/NiFe_2O_4/MIL-101(Fe)$ on the removal of MB was investigated. Solutions with a volume of 30 mL and a dye concentration of 25 mg L$^{-1}$ at natural pH (6.5–7) were used for this analysis. The adsorbent quantities tested were 15, 25 mg, 35 mg, and 45 mg. In the beginning, the efficiency of MB adsorption rises because of the larger specific surface area and abundant active adsorption sites. However, as time progresses, the vacated sites become occupied due to repulsions between the already adsorbed particles and the adsorbent particles.[45] Despite this, the adsorption capacity remains relatively constant when increasing the adsorbent dose while maintaining a constant initial concentration of pollutants. The removal percentages of

MB for the respective adsorbent doses of 15, 25, 35, and 45 mg were calculated to be 37, 98, 100, and 100%, respectively, within 24 minutes. In order to achieve the highest removal efficiency using the minimum amount of adsorbent, subsequent studies focused on utilizing 25 mg of $MoS_2/NiFe_2O_4/MIL-101(Fe)$.

**3.2.2 Effect of temperature on the dye adsorption.** In this research, we examined how temperature affects the adsorption of MB using the magnetic adsorbent $MoS_2/NiFe_2O_4/MIL-101(Fe)$ across a temperature range of 25 to 75 °C. The experimental conditions remained constant with 25 mg of the absorbent and a dye solution volume of 30 mL at natural pH of 6.5–7. The results are displayed in Fig. 10(b). It can be inferred from the results that the adsorption capacity increases as the temperature rises, which suggests the process is endothermic in nature. Probably due to the increase in temperature, the viscosity has decreased, which causes high mobility and faster diffusion of dye molecules on the surface and internal pores.

**3.2.3 Effect of initial dye concentration on the adsorption.** Fig. 10(c) shows the effect of initial dye concentration on adsorption by $MoS_2/NiFe_2O_4/MIL-101(Fe)$ composite. In these
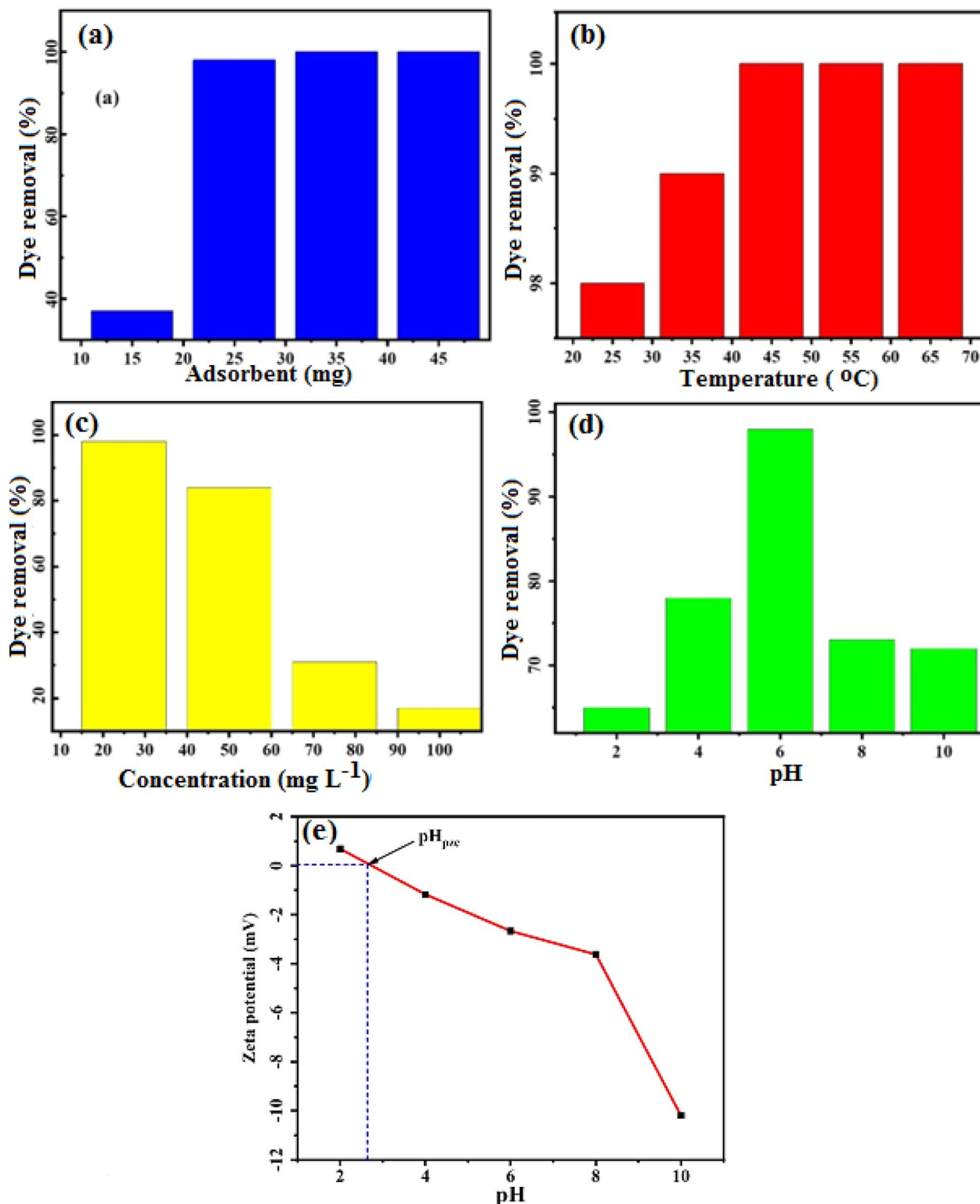
**Fig. 10** Influence of (a) adsorbent amount, (b) temperature, (c) dye concentration, (d) pH on the removal of MB dye by MoS$_2$/NiFe$_2$O$_4$/MIL-101(Fe), and (e) zeta potential of the MoS$_2$/NiFe$_2$O$_4$/MIL-101(Fe) nanocomposite in aqueous solutions at different pHs.

experiments, a range of dye concentrations were employed, including 25, 50, 75, 100, and 125 mg L$^{-1}$. The specific conditions included an MB concentration of 25 mg L$^{-1}$, pH 6.5–7, and a dye solution volume of 30 mL. With an increase in the initial

dye concentration, there was a corresponding decrease in the efficiency of dye elimination. This can be attributed to the fact that the active sites on the adsorbent saturated quickly in higher dye concentration. Consequently, an optimum concentration of
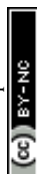
$25$ mg L$^{-1}$ was selected for MB in order to achieve maximum dye removal.

**3.2.4 Effect of pH on the dye adsorption.** The impact of varying pH levels ranging from 2 to 10 on the adsorption process of MB was investigated. Throughout the experiment, we maintained a consistent initial dye concentration of 25 mg L$^{-1}$ and a temperature of 25 °C. The solution pH was adjusted with HCl or NaOH. As depicted in Fig. 10(d), the nanocomposite exhibited varying adsorption rates for MB at different pH values. The highest dye absorption, reaching 98%, occurred at about natural pH (6.5–7). Conversely, the absorption percentages at pH 2, 4, 8, and 10 were found to be approximately 67, 81, 78, and 75%, respectively. As a result, at a natural pH (6.5–7), the electrostatic attraction between the nanocomposite and the MB dye is much stronger than at acidic and basic pHs. A cationic dye produces positively charged ions when dissolved in water. Hence, at lower pH levels, the hydrogen ion competes with the cationic MB species for adsorption onto the nanocomposite. With a higher concentration of H$^+$ ions on the absorbent surface, the adsorption of the MB cationic dye is prevented. Also, according to Fig. 10(e), the results obtained from the zeta potential of the composite show that the zeta potential of the composite is positive blow pH = 2.75, which can create electrostatic repulsion and prevent dye adsorption in acidic media. At pH higher than 2.75, the zeta potential of the nanocomposite is negative and the electrostatic attraction between the nanocomposite and the MB dye is much stronger than at stronger acidic/basic pHs. Alternatively, in higher pH conditions, the high concentration of OH$^-$ ions in the dye solution compete with the nanocomposite for the reaction with cationic MB, inhibiting the adsorption of MB dye.

**3.2.5 Selective dye adsorption.** The selective absorption and separation of specific dyes in the dye and wastewater treatment process is highly desirable. In this study, we investigated the selective adsorption capabilities of a nanocomposite material comprising MoS$_2$/NiFe$_2$O$_4$/MIL-101(Fe). To assess its performance, combinations of MB, RhB, and MO dye solutions were selected. The results in Fig. 11(a)–(d) show that both RhB
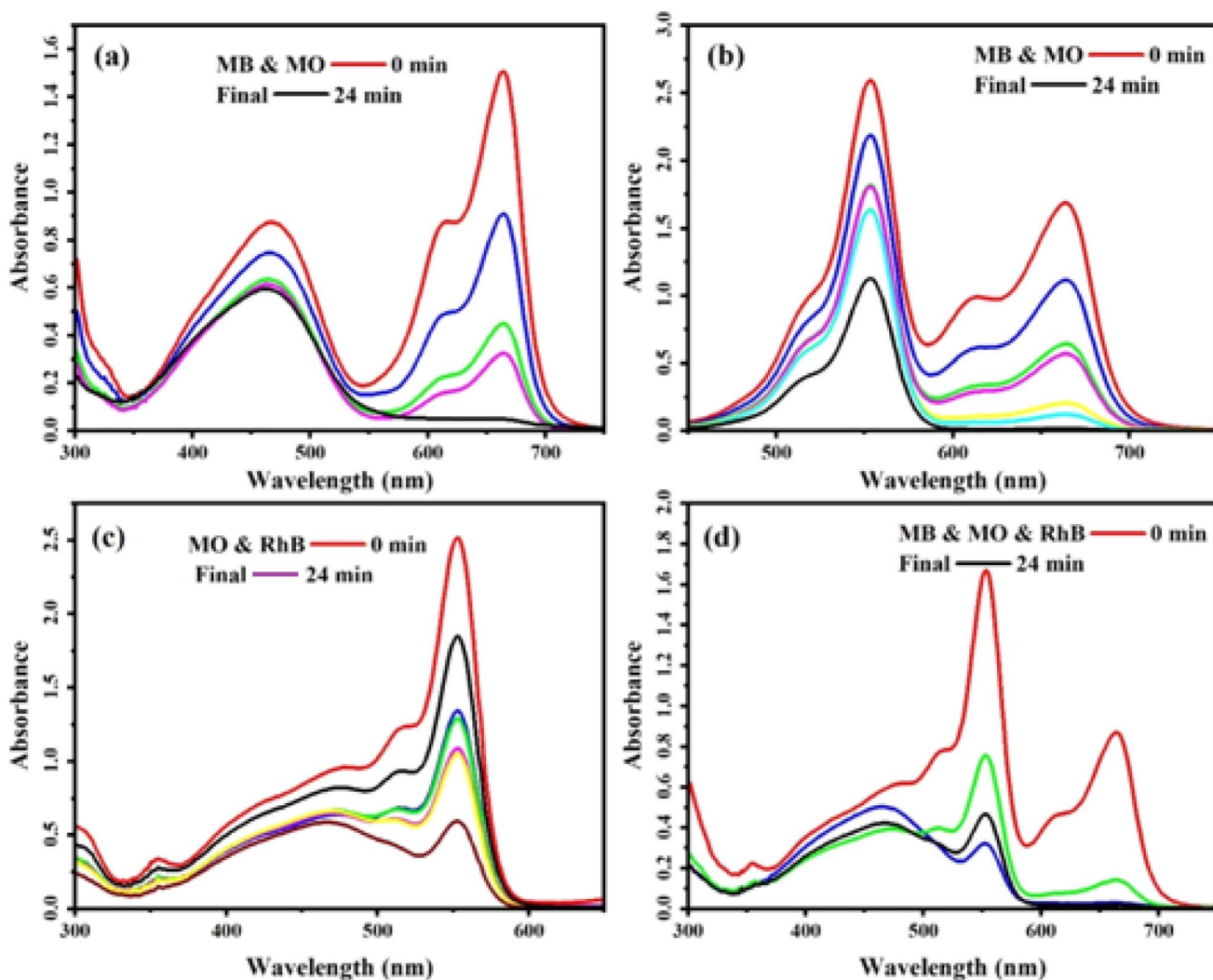


Fig. 11 The selective adsorption capacity of the MoS$_2$/NiFe$_2$O$_4$/MIL-101(Fe) toward the mixed dyes of (a) MB + MO, (b) MB + RhB, (c) MO + RhB, and (d) MB + MO + RhB. $C_{0(MB)} = C_{0(RhB)} = C_{0(MO)} = 25$ mg L$^{-1}$, and adsorbent dose = 25 mg in 30 mL, at 25 °C.

and MB dyes are adsorbed within 24 minutes, but complete adsorption of RhB needs a longer time. It is worth mentioning that the larger molecular structure of the RhB dye leads to a prolonged removal process compared to the MB dye. Interestingly, the characteristic peak of MO decreased slightly throughout the process. The results provide evidence of the nanocomposite's ability to selectively adsorb cationic dyes present in wastewater. Various factors can influence the adsorption mechanism of dye molecules onto the adsorbent employed in an aqueous environment. These factors include the properties of the adsorbent, the nature of the dye, intermolecular hydrogen interaction, electrostatic interaction, $\pi$–$\pi$ bonds, and ion exchange.[46] Initially, MIL-101 (Fe) exhibited limited effectiveness in removing cationic MB and RhB from the solution. However, the presence of $MoS_2$ in the nanocomposite significantly enhanced the removal efficiency. The increase in efficiency can be attributed to the electrostatic attraction between the negative charge of $MoS_2$ and the cationic MB and RhB molecules, leading to their effective removal. Fig. 8 showcased the zeta potential data, which corroborated that $MoS_2$ was the main influencing factor. The incorporation of $MoS_2$ nanosheets into the $MoS_2$/$NiFe_2O_4$MIL-101(Fe) nanocomposite further enhanced its adsorption ability for cationic MB and RhB. The reduced adsorption of RhB dye in comparison to MB could be due to the larger volume of RhB molecules, leading to steric hindrance at the adsorption sites and weak $\pi$–$\pi$ interactions. To remove this dye completely, a higher amount of nanocomposite would be required. On the other hand, the nanocomposite strongly rejects anionic MO dye.

## 3.3. Drug adsorption investigations

For the experimental analysis, TC and CIP were chosen as the specific antibiotics to assess the effectiveness of the $MoS_2$/$NiFe_2O_4$/MIL-101(Fe) nanocomposite in removing antibiotics from water contaminated with pollutants. The UV-vis absorption studies were conducted to determine the concentrations of TC and CIP. TC showed a maximum wavelength ($\lambda_{max}$) of 373 nm, while CIP exhibited a $\lambda_{max}$ of 337 nm. As depicted in Fig. 12, the absorption bands gradually declined over time, signifying a decrease in the drug concentration in the solution. After 24 minutes, the adsorption efficiency for TC reached approximately 95%, while CIP achieved an adsorption efficiency of around 90% after 36 minutes.

**3.3.1 Effect of adsorbent dose on the antibiotic adsorption.** The study investigated the influence of different amounts (15, 25, 35, and 45 mg) of $MoS_2$/$NiFe_2O_4$/MIL-101(Fe) adsorbent on the removal of TC and CIP from a 50 mL drug solution. The initial concentration of TC was 50 mg $L^{-1}$, while CIP had an initial concentration of 75 mg $L^{-1}$, both at pH 6.5–7. According to Fig. 13(a), it can be observed that as the dosage of the adsorbent increases, there is a corresponding increase in the removal of the drugs. More adsorption sites being available could be the reason for this.[47]

**3.3.2 Effect of temperature on the antibiotic adsorption.** The influence of different temperatures (25, 35, 45, 55, and 65 °C) on the removal efficiency of TC and CIP drugs from aqueous solutions was studied using $MoS_2$/$NiFe_2O_4$/MIL-101(Fe). The experimental conditions were maintained constant by utilizing 25 mg of adsorbent, a drug solution volume of 50 mL, a temperature of 25 °C, and a pH 6.5–7. The findings, depicted in Fig. 13(b), demonstrate that elevated temperatures increase the absorption rate, implying an endothermic adsorption process. The increase in temperature may lead to an increase in the diffusion rate of antibiotic molecules on the absorbent surface and occupy all the active sites of the absorbent surface.

**3.3.3 Effect of initial antibiotic concentration on the adsorption.** The effect of the various concentrations (25, 50, 75, 100, and 125 mg $L^{-1}$) of TC and CIP drugs on the adsorption efficiency of $MoS_2$/$NiFe_2O_4$/MIL-101(Fe) adsorbent under the constant conditions of 50 mg $L^{-1}$ absorbent, natural pH of 6.5–7, and 25 °C is shown in Fig. 13(c). As the initial drug concentration rises, there is a decline in drug removal. The decline
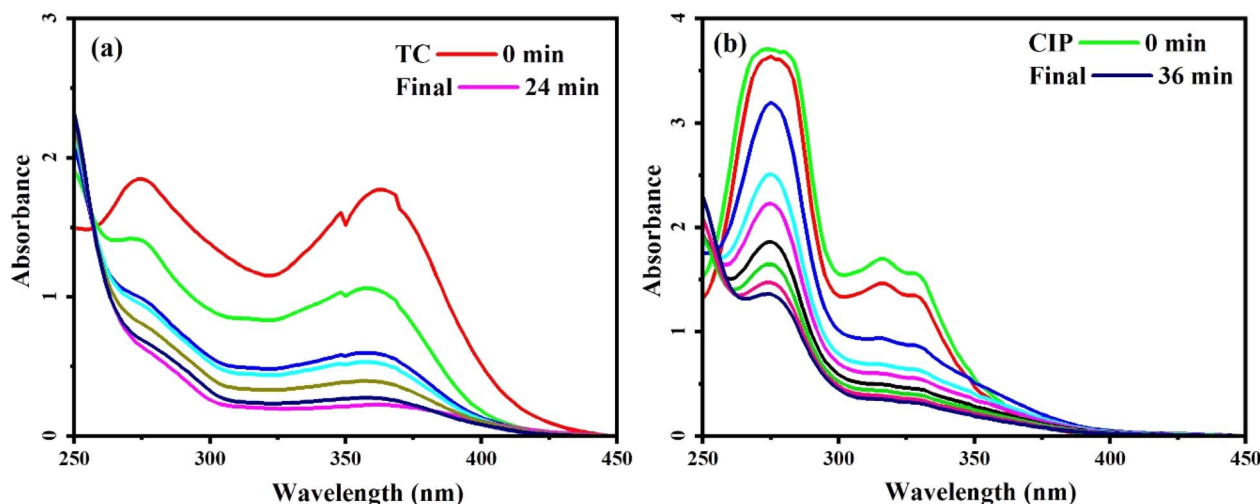


Fig. 12 UV-vis spectral changes of drugs aqueous solutions with $MoS_2$/$NiFe_2O_4$/MIL-101(Fe) at different time intervals: (a) TC and (b) CIP. Conditions: $C_{0(drug)}$ = 75 mg $L^{-1}$ for TC and 50 mg $L^{-1}$ for CIP, $V_{(drug)}$ = 50 mL, adsorbent dose = 25 mg at 25 °C.
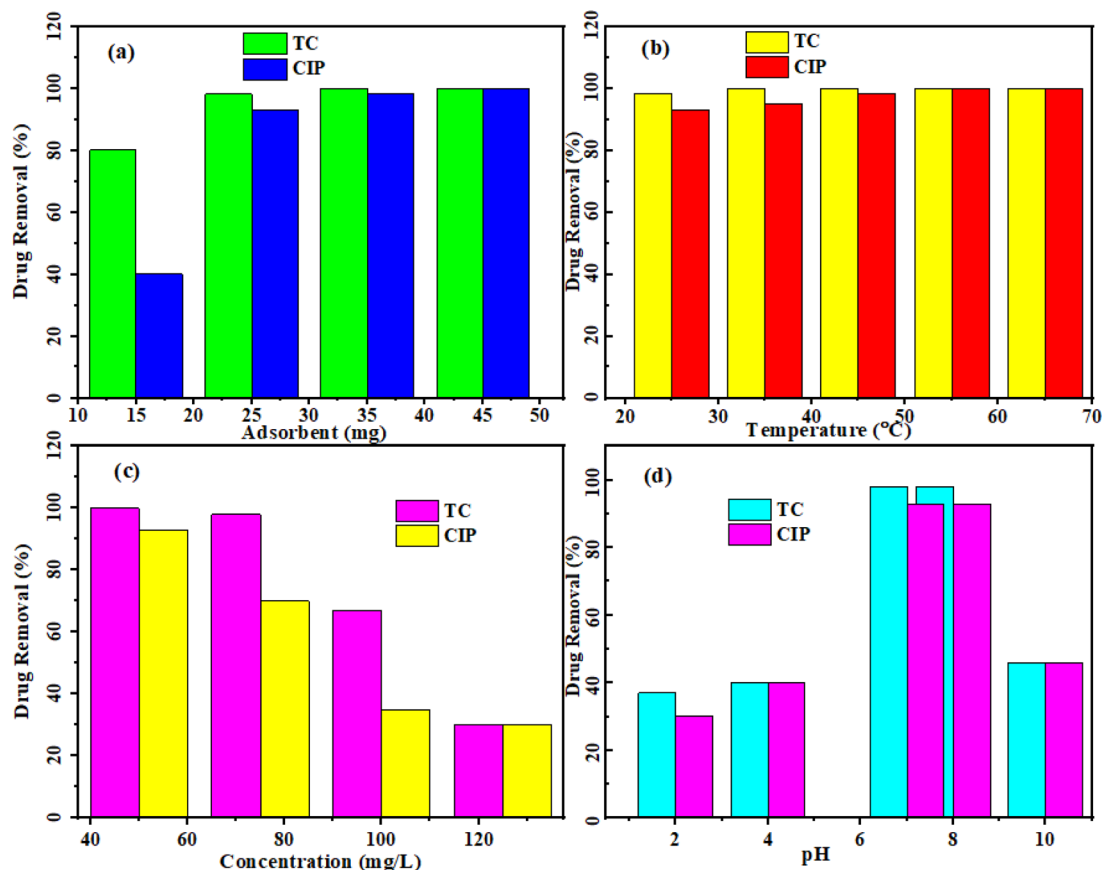
**Fig. 13** Influence of (a) adsorbent amount, (b) temperature, (c) concentration, and (d) pH on the removal of TC and CIP drugs by the MoS$_2$/NiFe$_2$O$_4$/MIL-101(Fe) nanocomposite.

observed can be attributed to a decrease in the number of active sites accessible for the adsorption, concomitant with the elevation in drug concentration. As the initial drug concentration rises, there is a decline in drug removal. The decline observed can be ascribed to a decrease in the number of active sites accessible for adsorption, concomitant with the elevation in drug concentration.

**3.3.4 Effect of pH on the antibiotic adsorption.** Changes in pH levels can affect the adsorbent composition, charge distribution, and differentiation of drug functional groups.[48] Within the pH range of 2 to 10, Fig. 13(d) presents the effect of pH on the removal of TC and CIP with initial concentrations of 75 mg L$^{-1}$ for TC and 50 mg L$^{-1}$ for CIP. The study involved investigating acidic conditions at pH levels of 2 and 4, as well as exploring alkaline conditions at pH levels of 8 and 10. At pH levels of 7 and 8, the greatest adsorption capacity for TC and CIP drugs was observed. The TC molecule displays the p$K_a$ values of 3.3, 7.7 and 9.7, indicating its ionization behavior at different pH levels. When the pH is below 3.3, TC adopts a cationic form known as TC$^+$. Between pH 3.3 and 7.7, it is zwitterionic (TC$^\pm$), while at pH levels of obove 7.7 and 9.7, it transforms to anionic TC$^-$/TC$^{-2}$ species. Likewise, the CIP molecule demonstrates two p$K_a$ values, namely 6.1 and 8.7. At pH levels below 6.1, CIP has cationic form. Between pH 6.1 and 8.7, it is zwitterionic (CIP$^\pm$), and above pH 8.7, it becomes anionic CIP$^-$/CIP$^{-2}$. The

solubility of TC and CIP is higher in acidic conditions, indicating lower drug absorption at pH 2. Conversely, when the pH exceeds 8, electrostatic repulsion occurs between the antibiotics and adsorbent, owing to their similar charges. This repulsive force acts as a barrier to the adsorption of drugs by the adsorbent. Consequently, the MoS$_2$/NiFe$_2$O$_4$/MIL-101(Fe) shows the maximum adsorption for TC and CIP drugs in their zwitterionic forms (TC$^\pm$ and CIP$^\pm$).

### 3.4. Adsorption efficiency of the nanocomposite components

To further demonstrate the role of MoS$_2$ in the composite material, the adsorption efficiency of MIL-101(Fe) and MoS$_2$ components for removing the different types of organic pollutants involving MB, MO, TC, and CIP from aqueous solutions at natural pH of 6.5–7 were investigated under the optimum reaction conditions. The UV-vis spectra of aqueous solutions of these pollutants in the presence of MIL-101(Fe) and MoS$_2$ as adsorbents are shown in Fig. 1S and 2S.† The results summarized in Fig. 14(a) and (b) indicate that the MIL-101(Fe) and MoS$_2$ components have lower removal efficiencies for the removal of different pollutants compared to the nanocomposite. As shown in Fig. 14(a), the removal rate of the individual MIL-101 was separately up to 18% for cationic dyes
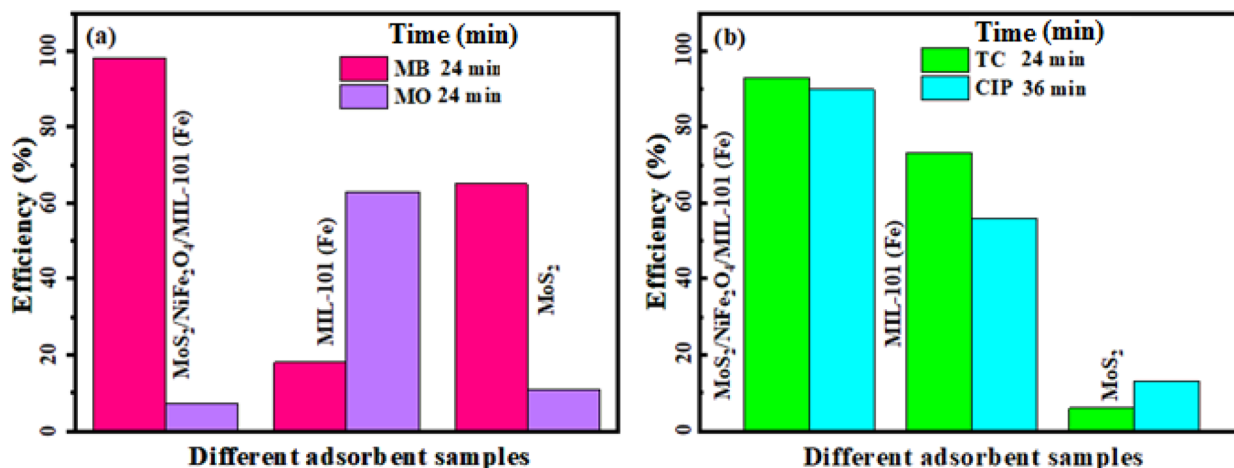
**Fig. 14** Comparison of removal efficiency of the nanocomposite with its components for (a) MB and MO dyes, and (b) TC and CIP drugs. Conditions: $C_{0(MB,MO)} = 50$ mg L$^{-1}$, $V_{(MB,MO)} = 30$ mL and $C_{0(TC)} = 75$ mg L$^{-1}$ and $V_{(TC)} = 50$ mL and $C_{0(CIP)} = 50$ mg L$^{-1}$, $V_{(CIP)} = 50$ mL, adsorbent dose $= 25$ mg at 25 °C.

MB, and 63% for anionic dye MO within 24 min. The reason for this phenomenon is that the framework of the MIL-101 is cationic with highly positive charge, as confirmed by zeta potential measurement (see Fig. 8). Nevertheless, the adsorption efficiency of $MoS_2$ with high negative zeta potential (see Fig. 8) was respectively able to reach 68% for cationic dyes MB, and 10% for anionic dye MO in the initial 24 min. Thus, as shown in Fig. 14(b) individual MIL-101 represented high adsorption capacity of 74% and 56% for TC and CIP drugs, respectively, whereas pure $MoS_2$ exhibited poor adsorption capacity for these drugs (less than 10%) probably due to highly aggregation of pure $MoS_2$ nanosheets that limited number of active sites. Especially, MIL-101 displayed higher adsorption capacity for TC, which is because of its smaller volume and more functional groups than CIP. Amazingly, after the introduction of $MoS_2$ into the cavity of MIL-101, the adsorption capacity of nanocomposite has changed a lot comparing with those of the isolated MIL-101MOF and pure $MoS_2$ nanosheets (Fig. 14(a) and (b)). This is probably because that $MoS_2$ nanosheets can be readily dispersed onto the surface of MIL-101 framework, leading to more active sites for the adsorption process. So, the $MoS_2$ functionalized MIL-101 frameworks could be selected and used as the active adsorbent for removing different pollutants. Then, the $MoS_2/NiFe_2O_4/MIL-101(Fe)$ nanocomposite material is an environmental friendly adsorbent for removing cationic organic pollutants after the introduction of $MoS_2$.

### 3.5. Adsorption kinetics and adsorption isotherm

By studying the adsorption isotherm, scientists can understand the equilibrium behavior of the adsorption process under different conditions. Two commonly used models to study adsorption isotherms are the Langmuir and Freundlich models. For adsorption on a uniform surface, the Langmuir isotherm is a suitable model for monolayer adsorption, assuming that the interactions between the adsorbed species are minimal. On the other hand, the Freundlich isotherm is established by the

adsorption of non-uniform layers on a heterogeneous surface. The adsorption isotherm equation allows us to mathematically model and predict the adsorption behavior under different operating conditions. The following equation represents the linear expression of the Langmuir isotherm (eqn (3)):[49]

$$\frac{c_e}{q_e} = \frac{1}{k_L q_m} + \frac{c_e}{q_m} \tag{3}$$

The value of $C_e$ (mg L$^{-1}$) corresponds to the concentration of dye or drug at equilibrium. In equations and models, the Langmuir adsorption constant is often denoted as $k_L$. The equilibrium concentration corresponds to $q_e$, which signifies the amount of dye or drug adsorbed per gram of adsorbent (mg g$^{-1}$). $q_m$ (mg g$^{-1}$) represents the maximum adsorption capacity achievable. An important characteristic of the Langmuir isotherm is the separation coefficient $R_L$, which indicates the level of desirability for adsorption onto an adsorbent. It is possible to determine it by employing the following equation (eqn (4)):[50]

$$R_L = \frac{1}{1 + k_L C_0} \tag{4}$$

$C_0$ represents the starting level of pollutant concentration. The $R_L$ factor provides information on the linearity ($R_L = 1$), irreversibility ($R_L = 0$), favorability ($0 < R_L < 1$), or unfavourability ($R_L > 1$ or $R_L < 0$) of the isotherm.[51] The following expression represents the Freundlich adsorption isotherm model (eqn (5)):[52]

$$\ln q_e = \ln k_f + \frac{1}{n} \ln C_e \tag{5}$$

The $n$ and $K_f$ constants refer to the Freundlich characteristic constants that represent the intensity and capacity (mg g$^{-1}$) of adsorption, respectively.

The Langmuir and Freundlich models were used to investigate experimental data. Fig. 3S(a)–(f)† show the Langmuir and Freundlich isotherms plots and the equilibrium data for MB, TC and CIP pollutants on the $MoS_2/NiFe_2O_4/MIL-101(Fe)$. The results are summarized in Table 2. According to the data in

**Table 2** The Langmuir and Freundlich models for MB, TC and CIP adsorption onto the $MoS_2/NiFe_2O_4/MIL-101(Fe)$ nanocomposite

| Dye and drug | Langmuir | | | | Freundlich | | |
|---|---|---|---|---|---|---|---|
| | $q_m$ (mg g$^{-1}$) | $K_L$ (L mg$^{-1}$) | $R^2$ | $R_L$ | $K_f$ (mg g$^{-1}$) | $n$ | $R^2$ |
| MB | 999.1 | 0.02502 | 0.930 | 0.615 | 1.011 | 1.019 | 0.999 |
| TC | 2991.3 | 0.02507 | 0.888 | 0.347 | 1.031 | 1.044 | 0.999 |
| CIP | 1994.2 | 0.02507 | 0.703 | 0.443 | 1.030 | 1.038 | 0.999 |

Table 2, the Freundlich isotherm model exhibits a higher correlation coefficient ($R^2$) compared to the Langmuir isotherm model. The experimental data exhibited a better fit with the Freundlich model. Therefore, the Freundlich isotherm model offers a more accurate depiction of adsorption behavior. The adsorption of three pollutants onto the $MoS_2/NiFe_2O_4/MIL-101$ (Fe) nanocomposite is favorable, as shown by the RL value of calculated for the initial dye and drag concentrations. In particular, for all pollutants, the constant value of $n$ was found to be close to 1, indicating a favorable adsorption process.

In order to investigate the mechanism of adsorption, the pseudo-first-order kinetics model and the pseudo-second-order kinetics model were used to test dynamical experimental data. The first-order reaction model is expressed as follows (eqn (6)):

$$\ln(q_e - q_t) = \ln q_e - \frac{k_1}{2.303} \tag{6}$$

where $k_1$ is the pseudo-first-order adsorption rate constant (min$^{-1}$). The values of $k_1$ and $q_e$ were determined from the slope and intercept of the plots of $\ln(q_e - q_t)$ versus $t$. Another kinetic model introduced in the literature is the pseudo-second-order model, which is expressed as the following equation (eqn (7)):

$$\frac{t}{q_t} = \left(\frac{t}{k_2 q_e^2}\right) + \left(\frac{t}{q_e}\right) \tag{7}$$

where $k_2$ (g mg$^{-1}$ min$^{-1}$) is a pseudo-second-order rate constant. $k_2$ is calculated from the intercept of the plot of $t/q_t$ versus $t$, and used to estimate the values of $q_e$ (cal.) and $k_2$. $q_e$ (mg g$^{-1}$) and $q_t$ (mg g$^{-1}$) are the adsorption amounts of dye and drug at equilibrium and at time $t$, respectively.

The adsorption kinetics of MB, TC and CIP were investigated by using pseudo-first-order and pseudo-second-order models.

Fig. 4S(a)–(f)† show the plots of the pseudo-first-order and pseudo-second-order kinetics. The corresponding kinetic parameters obtained from two models ($k_1$, $k_2$, $q_e$cal and $R^2$) are listed in Table 3. It can be seen that the fitting of experimental data to the pseudo-first-order model was not so good, with rather low correlation coefficients ($R^2$). Accordingly, the experimental data did not obey the pseudo-first-order kinetic model. Conversely, linear plots of $t/q_t$ versus $t$ with correlation coefficients higher than 0.997 indicated that the data exhibited good compliance with the pseudo-second-order kinetic equation. According to the values of $R^2$, it is obvious that the adsorption kinetics of MB, TC and CIP followed the pseudo-second-order kinetic model.

### 3.6. Adsorption thermodynamics

Thermodynamic studies are one of the important parameters in studying the absorption process. During the thermodynamic experiments, adsorption experiments were performed under different temperature conditions to analyze their effects. The investigated parameters include enthalpy ($\Delta H°$), entropy ($\Delta S°$), and Gibbs free energy ($\Delta G°$). The thermodynamic adsorption equations are shown below.

$$k_c = \frac{q_e}{c_e} \tag{8}$$

$$\Delta G° = -RT \ln K_c \tag{9}$$

$$\ln K_c = \frac{\Delta S°}{R} - \frac{\Delta H°}{RT} \tag{10}$$

where $\Delta H°$ (kJ mol$^{-1}$), $\Delta G°$ (kJ mol$^{-1}$), and $\Delta S°$ (kJ mol$^{-1}$ K$^{-1}$) are the standard enthalpy change, standard Gibbs free energy

**Table 3** Kinetics parameters for MB, TC, and CIP adsorption

| Pseudo first order kinetic model | $q_e$, exp (mg g$^{-1}$) | $q_e$, cal (mg g$^{-1}$) | $k_1$ (min$^{-1}$) | $R^2$ |
|---|---|---|---|---|
| MB | 82.47 | 0.001 | 0.002 | 0.444 |
| TC | 93.15 | 0.004 | 0.069 | 0.975 |
| CIP | 67.62 | 0.007 | 0.056 | 0.897 |

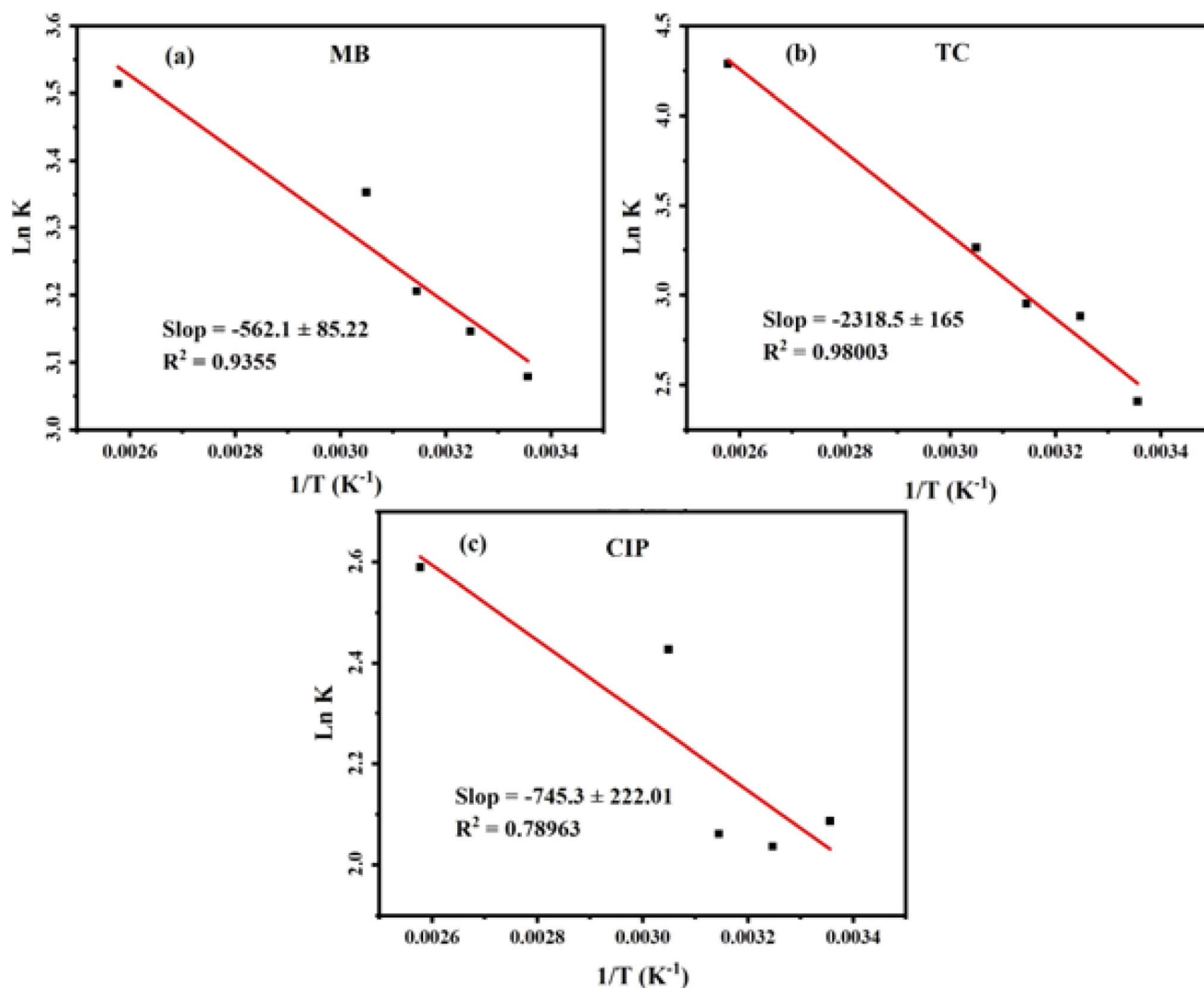| Pseudo second order kinetic model | Initial con. (mg L$^{-1}$) | $k_2$ (g mg$^{-1}$ min$^{-1}$) | $q_e$, cal (mg g$^{-1}$) | $R^2$ |
|---|---|---|---|---|
| MB | 75 | 0.0001 | 51.62 | 0.999 |
| TC | 100 | 0.0001 | 52.05 | 0.998 |
| CIP | 100 | 0.0001 | 65.18 | 0.998 |

**Fig. 15** Van't Hoff plots for the adsorption process of (a) MB dye, (b) TC and (c) CIP drugs onto the $MoS_2/NiFe_2O_4/MIL$-101(Fe) nanocomposite.

change, and standard entropy change, respectively. $T$ (K) represents the absolute temperature, $R$ (8.314 J mol$^{-1}$ K$^{-1}$) is the gas constant, $K_c$ is the distribution coefficient, $q_e$ is the adsorption capacity, and $C_e$ is the solution concentration at the equilibrium state. From Fig. 15, the $\Delta H°$ and $\Delta S°$ values for MB dye and two TC and CIP drugs can be obtained from the slope and intercept of van't Hoff plots, respectively. Based on the data presented in Table 4, the positive $\Delta H°$ values suggest that the adsorption process of dye and drugs onto the $MoS_2/NiFe_2O_4/$ MIL-101(Fe) nanocomposite is endothermic in nature.

### 3.7. Adsorption mechanism

The adsorption efficiency of the $MoS_2/NiFe_2O_4/MIL$-101(Fe) nanocomposite has been found to be more effective in drug and dye absorption compared to individual components such as $MoS_2$, $NiFe_2O_4$, and MIL-101(Fe). This increased effectiveness can be attributed to the larger adsorbent surface area, which provides more active sites for adsorption activities. The results of the investigations showed that the drug and dye adsorption

**Table 4** Thermodynamic Parameters of MB, TC and CIP adsorption onto the $MoS_2/NiFe_2O4/MIL$-101(Fe) nanocomposite

| Dye/drug | $T$ (K) | $\Delta G°$ (kJ mol$^{-1}$) | $\Delta H°$ (kJ mol$^{-1}$) | $\Delta S°$ (kJ mol$^{-1}$ K$^{-1}$) |
|---|---|---|---|---|
| MB | 298 | −11.01 | 4.67 | 708.5 |
| | 308 | −11.38 | | |
| | 318 | −11.75 | | |
| | 328 | −12.12 | | |
| | 338 | −12.49 | | |
| TC | 298 | −12.65 | 19.27 | 1371.8 |
| | 308 | −13.07 | | |
| | 318 | −13.49 | | |
| | 328 | −13.92 | | |
| | 338 | −14.34 | | |
| CIP | 298 | −13.38 | 6.19 | 1845.7 |
| | 308 | −13.83 | | |
| | 318 | −14.25 | | |
| | 328 | −14.73 | | |
| | 338 | −15.18 | | |

reaction is an endothermic process and is performed with better efficiency at higher temperatures. Drug molecules have a conjugated benzene ring structure. Therefore, the π–π stacking interaction increases the adsorption capacity of the materials during the adsorption process. The presence of functional groups in drugs, such as OH, $NH_2$, carbonyl groups, and the MIL-101(Fe) carboxylate group, allows for hydrogen bonding with the nanocomposite. Adsorption of TC and CIP on the adsorbent mainly takes place through electrostatic interaction and π–π stacking. In addition, MB is a cationic dye that is positively charged in an aqueous solution. This confirms that other factors, besides the specific surface area of the adsorbent, affect the adsorption efficiency. This is due to the rapid and effective adsorption of MB cationic dye by $MoS_2$ nanosheets. However, the adsorption of the anionic dye MO is unfavorable for $MoS_2/NiFe_2O_4/MIL-101(Fe)$. Zeta potentials of MIL-101(Fe), $MoS_2$, and $MoS_2/NiFe_2O_4/MIL-101(Fe)$ samples were measured as +32.4, −47.0, and −19.8 mV in water in a natural pH (6.5–7), respectively. After modification with $MoS_2$, the $MoS_2/NiFe_2O_4/MIL-101(Fe)$ nanocomposite showed a more negative zeta potential than the pristine MIL-101(Fe); therefore, it can absorb more cationic dyes such as MB, while the adsorption of anionic dyes such as MO is unfavorable. To better understand adsorption process, the surface charge of $MoS_2/NiFe_2O_4/MIL-101(Fe)$ composite at different pHs was measured (see Fig. 10(e)). For comparison, the zeta potential of nascent $MoS_2$ and MIL-

**Table 5** Comparison of the adsorption capacity of various adsorbents for MB, TC and CIP pollutants

| Adsorbents | Adsorbate | $q_m$ (mg g$^{-1}$) | Ref. |
|---|---|---|---|
| CuS@PANI/PW$_{12}$ | MB | 83.3 | 53 |
| Fe$_3$O$_4$@AMCA-MIL53 (Al) | MB | 325 | 54 |
| Activated lignin–chitosan | MB | 34.7 | 55 |
| MOF-235 | MB | 187 | 56 |
| H$_3$PW$_{12}$O$_{40}$/MIL-101(Fe) | MB | 473.7 | 57 |
| CDF/MF | TC | 168.24 | 58 |
| MnFe$_2$O$_4$/rGO | TC | 41 | 59 |
| MWCNT-MIL-53 (Fe) | TC | 180.68 | 60 |
| CNT/b-CD/MnFe$_2$O$_4$ | TC | 89.53 | 61 |
| CoO@C | TC | 769.43 | 62 |
| Fe$_3$O$_4$/cellulose | CIP | 6.9 | 63 |
| CS-g-PA/TSM | CIP | 238.3 | 64 |
| MIL101 (Cr)–HSO$_3$ | CIP | 564.9 | 65 |
| c-FD | CIP | 328 | 66 |
| Ga-cl-PAM/C3N4 | CIP | 169.49 | 67 |
| MoS$_2$/NiFe$_2$O$_4$/MIL-101(Fe) | MB | 999.1 | This work |
| MoS$_2$/NiFe$_2$O$_4$/MIL-101(Fe) | TC | 2991.3 | This work |
| MoS$_2$/NiFe$_2$O$_4$/MIL-101(Fe) | CIP | 1994.2 | This work |

101(Fe) were also presented in Fig. 8. The results of zeta potential of the $MoS_2/NiFe_2O_4/MIL-101(Fe)$ composite in Fig. 10(e) indicate that at pH values below 2.75, the $MoS_2/NiFe_2O_4/MIL-101(Fe)$ surface was positively resulting in weaker interaction between the surface groups and cationic dyes and
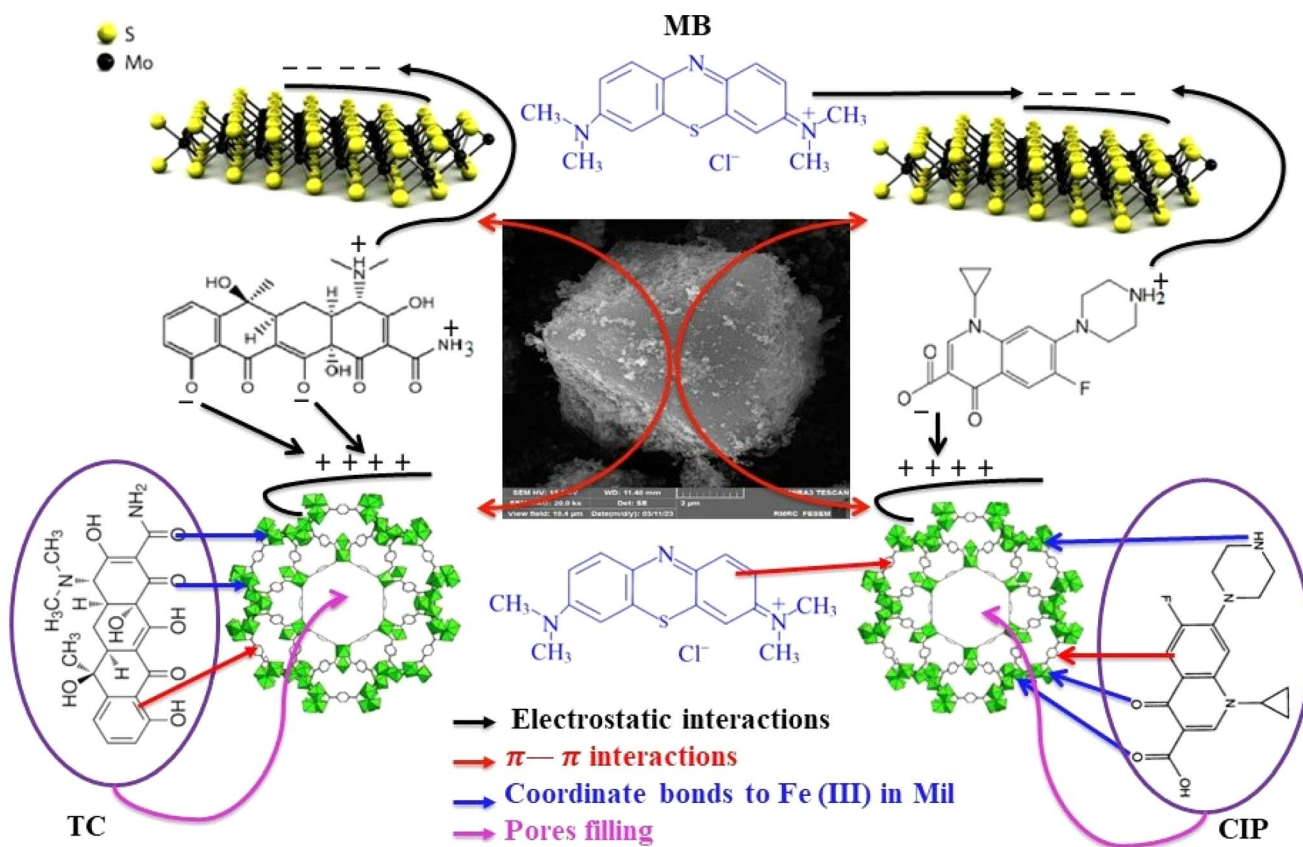


**Scheme 1** Possible mechanism for the adsorption of drugs and dyes onto the $MoS_2/NiFe_2O_4/MIL-101(Fe)$ nanocomposite.

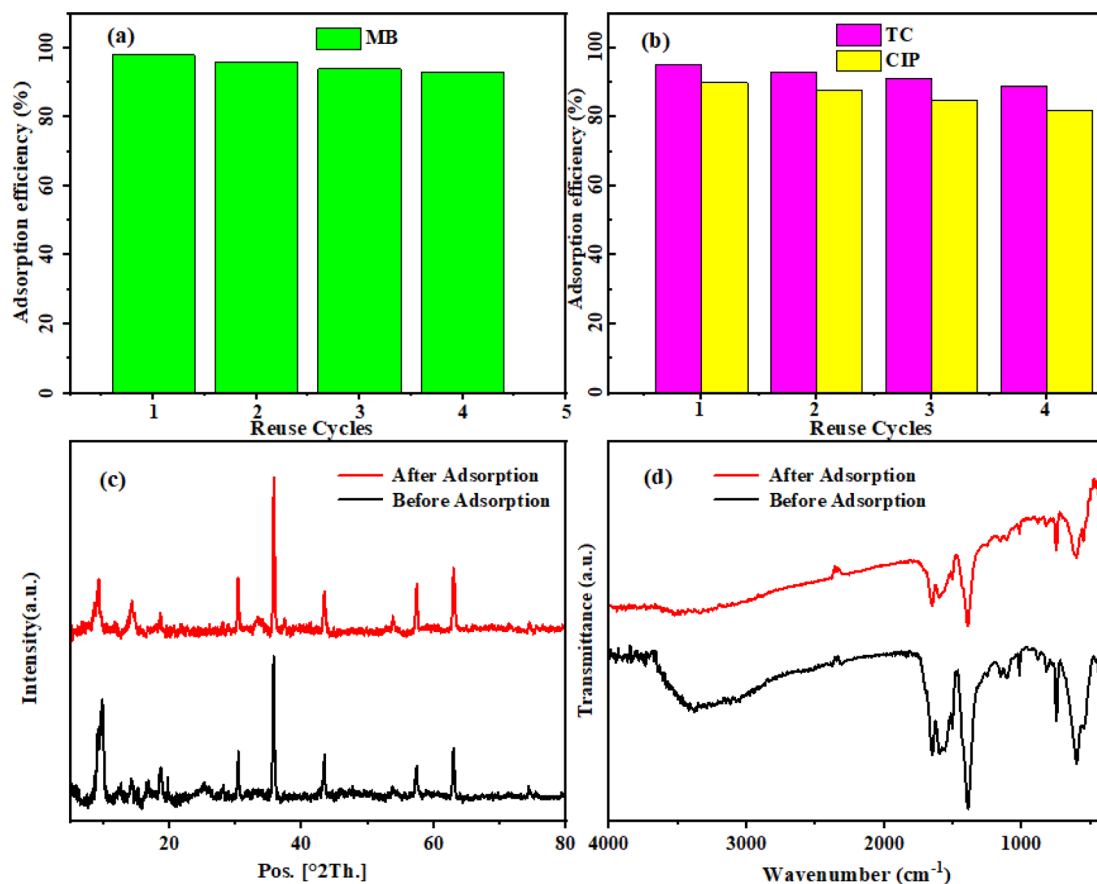**Fig. 16** Reusability of the MoS$_2$/NiFe$_2$O$_4$/MIL-101(Fe) in the removal of (a) MB dye, (b) TC and CIP drugs, (c) X-ray diffraction patterns and (d) FTIR spectra before and after adsorption.

drugs and above pH 2.7, the presence of negative charge on the surface of MoS$_2$/NiFe$_2$O$_4$/MIL-101(Fe) hybrid material, leading to the efficient adsorption of cationic MB dyes and for TC and CIP drugs in their zwitterionic forms (TC$^{\pm}$ and CIP$^{\pm}$). In conclusion, the electrostatic interactions are the primary adsorption mechanism for dyes and drugs. The simplified mechanism of drug and dye adsorption is depicted in Scheme 1.

### 3.8. Comparison with other reported adsorbents

To showcase the superiority of the current adsorbent, we conducted a comparative analysis of its effectiveness in removing MB, TC, and CIP from aqueous solutions. This evaluation was done in relation to similar adsorbents, as documented in Table 5.[53–67] Based on the data, the MoS$_2$/NiFe$_2$O$_4$/MIL-101(Fe) adsorbent demonstrates a higher adsorption capacity for the removal of dyes and drugs compared to the majority of other adsorbents reported in the scientific literature.

### 3.9. Stability and recyclability

The practical application of an adsorbent depends on its reusability and stability. The reutilization potential of the MoS$_2$/NiFe$_2$O$_4$/MIL-101(Fe) nanocomposite was examined in this research through four successive cycle tests conducted under identical conditions. The results demonstrated a diminishing

trend in removal efficacy during the first three cycles (Fig. 16(a) and (b)), which can be attributed to the chemisorption phenomenon. However, after the third cycle, the elimination efficiency remained relatively constant, indicating that the absorbent had reached saturation and further absorption was not possible. Nevertheless, the removal efficiency of MoS$_2$/NiFe$_2$O$_4$/MIL-101(Fe) for MB, TC, and CIP remained above 80% even after four cycles, demonstrating its good regenerability and reusability as well as its potential in practical applications. Furthermore, XRD and FT-IR analysis (Fig. 16(c) and (d)) were performed on the nanocomposite before and after adsorption. The conducted analyses demonstrated the magnetic nanocomposite's structural stability throughout the adsorption process, indicating its resistance to solvents, drugs, and dyes.

## 4. Conclusion

The hydrothermal method was used to synthesize a magnetic nanocomposite consisting of MoS$_2$/NiFe$_2$O$_4$/MIL-101(Fe). The objective of this research was to investigate the adsorption potential of the nanocomposite for effectively removing both dyes and drugs from aqueous solutions. The adsorption capacities of MoS$_2$/NiFe$_2$O$_4$/MIL-101(Fe) for MB, TC, and CIP were determined to be 999.1, 2991.3, and 1994.2 mg g$^{-1}$, respectively. The pseudo-second-order model and Freundlich

model are considered to be suitable for describing the adsorption behavior of $MoS_2/NiFe_2O_4/MIL-101(Fe)$. Notably, even after four recycling cycles, the $MoS_2/NiFe_2O_4/MIL-101(Fe)$ nanocomposite demonstrated a removal efficiency of over 80% for MB, TC, and CIP, indicating its potential for practical applications due to its good recyclability and reusability. Remarkably, this material exhibited a high adsorption capacity for pollutants. Hence, it is a promising and environmental friendly adsorbent for removing and separating organic pollutants from wastewater.

## Conflicts of interest

There are no conflicts to declare.

## Acknowledgements

## References

1 A. Ajmal, I. Majeed, R. N. Malik, H. Idriss and M. A. Nadeem, *RSC Adv.*, 2014, **4**, 37003–37026.

2 G. Sharma, D. D. Dionysiou, S. Sharma, A. Kumar, H. Ala'a, M. Naushad and F. J. Stadler, *Catal. Today*, 2019, **335**, 437–451.

3 S. Samsami, M. Mohamadizaniani, M. H. Sarrafzadeh, E. R. Rene and M. Firoozbahr, *Process Saf. Environ. Prot.*, 2020, **143**, 138–163.

4 J. Yang, M. Zhu and D. D. Dionysiou, *Water Res.*, 2021, **189**, 116627.

5 E. Routoula and S. V. Patwardhan, *Environ. Sci. Technol.*, 2020, **54**, 647–664.

6 H. Fattahimoghaddam, T. Mahvelati-Shamsabadi and B. K. Lee, *J. Hazard. Mater.*, 2021, **403**, 123703.

7 J. Abdi, M. Vossoughi, N. M. Mahmoodi and I. Alemzadeh, *Chem. Eng. J.*, 2017, **326**, 1145–1158.

8 G. Crini, *Bioresour. Technol.*, 2006, **97**, 1061–1085.

9 A. Javid, A. Mesdaghinia, S. Nasseri, A. H. Mahvi, M. Alimohammadi and H. Gharibi, *J. Environ. Health Sci. Eng.*, 2016, **14**, 1–5.

10 R. Trujillano, V. Rives and I. García, *Molecules*, 2022, **9**, 2904.

11 Z. Song, Y.-L. Ma and C.-E. Li, *Sci. Total Environ.*, 2019, **651**, 580–590.

12 M. Ågerstrand, C. Berg, B. Björlenius, M. Breitholtz, B. Brunström, J. Fick, L. Gunnarsson, D. G. Joakim Larsson, J. P. Sumpter, M. Tysklind and C. Rudén, *Environ. Sci. Technol.*, 2015, **49**, 5336–5345.

13 A. A. Isari, M. Mehregan, S. Mehregan, F. Hayati, R. Rezaei Kalantary and B. Kakavandi, *J. Hazard. Mater.*, 2020, **390**, 122050.

14 W. Song, T. Yang, X. Wang, Y. Sun, Y. Ai, G. Sheng and X. Wang, *Environ. Sci.: Nano*, 2016, **3**, 1318–1326.

15 H. Chen, B. Gao and H. Li, *J. Hazard. Mater.*, 2015, **282**, 201–207.

16 B. Fan, Y. Tan, J. Wang, B. Zhang, Y. Peng, C. Yuan and S. Cui, *Processes*, 2021, **9**, 1644.

17 C. Zhang, X. Han, F. Wang, L. Wang and J. Liang, *Front. Chem.*, 2021, **9**, 736369.

18 M. Cao, P. Wang, Y. Ao, C. Wang, J. Hou and J. Qian, *J. Colloid Interface Sci.*, 2016, **467**, 129–139.

19 Y. Li, L. Chen, Y. Wang and L. Zhu, *Mater. Sci. Eng. B*, 2016, **210**, 29–36.

20 H. T. Chandran, S. Thangavel, C. V. Jipsa and andG. Venugopal, *Mater. Sci. Semicond. Process.*, 2014, **27**, 212–219.

21 N. Javid, Z. Honarmandrad and M. Malakootian, *Desalin. Water Treat.*, 2020, **174**, 178–185.

22 J. Chen, Y. S. Liu, J. N. Zhang, Y. Q. Yang, L. X. Hu, Y. Y. Yang and G. G. Ying, *Bioresour. Technol.*, 2017, **238**, 70–77.

23 Y. Gao, Y. Li, L. Zhang, H. Huang, J. Hu, S. M. Shah and X. Su, *J. Colloid Interface Sci.*, 2012, **368**, 540–546.

24 H. Li, D. Zhang, X. Han and B. Xing, *Chemosphere*, 2014, **95**, 150–155.

25 X. R. Jing, Y. Y. Wang, W. J. Liu, Y. K. Wang and H. Jiang, *Chem. Eng. J.*, 2014, **248**, 168–174.

26 P. Zhao, M. Jian, Q. Zhang, R. Xu, R. Liu, X. Zhang and H. Liu, *J. Mater. Chem. A*, 2019, **7**, 16598–16621.

27 Y. J. Yuan, Z. Shen, S. Wu, Y. Su, L. Pei, Z. Ji and Z. Zou, *Appl. Catal., B*, 2019, **246**, 120–128.

28 A. A. Isari, A. Payan, M. Fattahi, S. Jorfi and B. Kakavandi, *Appl. Surf. Sci.*, 2018, **462**, 549–564.

29 S. Silvestri, J. F. de Oliveira and E. L. Foletto, *Mater. Res. Bull.*, 2019, **117**, 56–62.

30 D. Chiappe, E. Scalise, E. Cinquanta, C. Grazianetti, B. van den Broek, M. Fanciulli and A. Molle, *Adv. Mater.*, 2014, **26**, 2096–2101.

31 U. Krishnan, M. Kaur, K. Singh, M. Kumar and A. Kumar, *Superlattices Microstruct.*, 2019, **128**, 274–297.

32 Q. Zhang, Y. Cui and G. Qian, *Coord. Chem.*, 2019, **378**, 310–332.

33 X. Han, H. G. Godfrey, L. Briggs, A. J. Davies, Y. Cheng, L. L. Daemen and M. Schröder, *Nat. Mater.*, 2018, **17**, 691–696.

34 J. Lee, C. Y. Chuah, J. Kim, Y. Kim, N. Ko, Y. Seo and E. Lee, *Angew. Chem., Int. Ed.*, 2018, **130**, 7995–7999.

35 X. Zhao, Y. Wang, D. S. Li, X. Bu and P. Feng, *Adv. Mater.*, 2018, **30**, 1705189.

36 L. Yue, X. Wang, T. Sun, T. Liu, Q. Li, N. Wu and W. Yang, *Chem. Eng. J.*, 2019, **375**, 121959.

37 D. Zhu, J. Liu, Y. Zhao, Y. Zheng and S. Z. Qiao, *Small*, 2019, **15**, 1805511.

38 N. M. Mahmoodi, J. Abdi, M. Oveisi, M. A. Asli and M. Vossoughi, *Mater. Res.*, 2018, **100**, 357–366.

39 C. F. Zhang, L. G. Qiu, F. Ke, Y. J. Zhu, Y. P. Yuan, G. S. Xu and X. Jiang, *J. Mater. Chem. A*, 2013, **1**, 14329–14334.

40 P. L. Hariani, M. Said, A. Rachmat, F. Riyanti, H. C. Pratiwi and W. T. Rizk, *Bull. Chem. React. Eng. Catal.*, 2021, **16**, 481–490.

41 A. Hamedi, F. Trotta, M. Borhani Zarandi, M. Zanetti, F. Caldera, A. Anceschi and M. R. Nateghi, *Int. J. Mol. Sci.*, 2019, **20**, 5612.

42  Z. Liu, W. He, Q. Zhang, H. Shapour and M. F. Bakhtari, *ACS Omega*, 2021, **6**, 4597–4608.

43  H. K. Sadhanala, S. Senapati, K. V. Harika, K. K. Nanda and A. Gedanken, *New J. Chem.*, 2018, **42**, 14318–14324.

44  K. Zhou, S. Jiang, C. Bao, L. Song, B. Wang, G. Tang and Z. Gui, *RSC Adv.*, 2012, **2**, 11695–11703.

45  G. S. Dos Reis, B. G. Cazacliu, C. R. Correa, E. Ovsyannikova, A. Kruse, C. H. Sampaio and G. L. Dotto, *J. Environ. Chem. Eng.*, 2020, **8**, 103605.

46  G. P. Hao, W. C. Li, S. Wang, S. Zhang and A. H. Lu, *Carbon*, 2010, **48**, 3330–3339.

47  M. Beiranvand, S. Farhadi and A. Mohammadi-Gholami, *RSC Adv.*, 2022, **12**, 34438–34453.

48  S. Bazgir, S. Farhadi and Y. Mansourpanah, *J. Solid State Chem.*, 2022, **315**, 123513.

49  A. A. Hoseini, S. Farhadi, A. Zabardasti and F. Siadatnasab, *RSC Adv.*, 2020, **10**, 40005–40018.

50  C. Jiao, Y. Wang, M. Li, Q. Wu, C. Wang and Z. Wang, *J. Magn. Magn. Mater.*, 2016, **407**, 24–30.

51  A. Jarrah and S. Farhadi, *J. Solid State Chem.*, 2020, **285**, 121264.

52  X. Liu, W. Gong, J. Luo, C. Zou, Y. Yang and S. Yang, *Appl. Surf. Sci.*, 2016, **362**, 517–524.

53  F. Siadatnasab, K. Karami and A. Khataee, *J. Ind. Eng. Chem.*, 2019, **80**, 205–216.

54  A. A. Alqadami, M. Naushad, Z. A. Alothman and T. Ahamad, *J. Environ. Manage.*, 2018, **223**, 29–36.

55  A. B. Albadarin, M. N. Collins, M. Naushad, S. Shirazian, G. Walker and C. Mangwandi, *Chem. Eng. J.*, 2017, **307**, 264–272.

56  E. Haque, J. W. Jun and S. H. Jhung, *J. Hazard. Mater.*, 2011, **185**, 507–511.

57  T. T. Zhu, Z. M. Zhang, W. L. Chen, Z. J. Liu and E. B. Wang, *RSC Adv.*, 2016, **6**, 81622–81630.

58  T. Ahamad, R. Chaudhary, A. A. Naushad and M. Alshehri, *Int. J. Biol. Macromol.*, 2019, **134**, 180–188.

59  J. Bao, Y. Zhu, S. Yuan, F. Wang, H. Tang, Z. Bao and Y. Chen, *Nanoscale Res. Lett.*, 2018, **13**, 1–8.

60  W. Xiong, G. Zeng, Z. Yang, Y. Zhou, C. Zhang, M. Cheng and X. Li, *Sci. Total Environ.*, 2018, **627**, 235–244.

61  R. Foroutan, S. J. Peighambardoust, P. Latifi, A. Ahmadi, M. Alizadeh and B. Ramavandi, *J. Environ. Chem. Eng.*, 2021, **9**, 106344.

62  G. Yang, Q. Gao, S. Yang, S. Yin, X. Cai, X. Yu and Y. Fang, *Chemosphere*, 2020, **239**, 124831.

63  A. Azizi, *J. Iran. Chem. Soc.*, 2021, **18**, 331–341.

64  Y. K. Manea, A. M. Khan, A. A. Wani, M. T. Qashqoosh, M. Shahadat and M. A. Salem, *J. Mol. Liq.*, 2021, **335**, 116144.

65  Z. Li, M. Ma, S. Zhang, Z. Zhang, L. Zhou, J. Yun and R. Liu, *J. Porous Mater.*, 2020, **27**, 189–204.

66  A. Jain, A. Sharma, A. Kapur, S. Wadhawan, M. Garg, S. K. Pandey and S. K. Mehta, *J. Nanostruct. Chem.*, 2021, **11**, 437–453.

67  G. Sharma, A. Kumar, M. Naushad, B. Thakur, D. V. N. Vo, B. Gao and F. J. Stadler, *J. Hazard. Mater.*, 2021, **416**, 125714.